Variational phase-field fracture modeling with interfaces

Keita Yoshioka[a,], Mostafa Mollaali[a], Olaf Kolditz[a,b]

[a]Department of Environmental Informatics, Helmholtz Centre for Environmental Research – UFZ, Leipzig, Germany
[b]Applied Environmental Systems Analysis, Technische Universität Dresden, Dresden, Germany

Abstract

This paper proposes a diffused approach to approximate failure at interfaces that physically occupy negligible space compared to the bulk material. For an interface diffused over a certain length, we derive an effective interface fracture toughness based on the diffused length and the fracture toughness of the bulk and the interface. Our derivation ensures the energetic equivalence between the sharp and the diffused representations of interface.

We verified the critical energy release rates in a steadily propagating tensile fracture example as well as the critical fracture pressure and the crack length evolution in toughness dominated hydraulic fracturing. The proposed model does not require any changes in existing implementation of phase-field models. The only requirement is to assign the analytically calculated effective interface fracture toughness over a diffused sub-domain.

Keywords: phase-field; interface failure; hydraulic fracture; natural fracture; OpenGeoSys

1. Introduction

Phase-field models for fracture have become one of the most standard methods for simulation of fracturing which enjoy wide applicability from brittle [12, 61, 62], ductile [1, 3, 46, 85], dynamic [10, 14, 53, 66], fatigue [18, 73], dessication [17, 40, 58], environment assisted [23, 57, 72] and to hydraulic fracturing [11, 20, 28, 39, 71, 81] to list just a few. This popularity is attributed by their capability to model complex evolution of an arbitrary number of cracks without restricting their propagation to any specific grid.

Weak or strong, interfaces impact fracture evolution. Failure tends to concentrate at interfaces in fiber reinforced cement (FRC) composites [26, 51] and composite laminates [89]. For geological materials, pre-existing interfaces (*e.g.* natural fractures or faults) alter hydraulic fracture paths in many ways [84] (Fig. 1). Like fractures, such material interface occupies essentially negligible domain. Thus, diffused treatment of fracture in the phase-field models have also been applied to interface modeling.

Existing studies may be categorized into two approaches. One approach is to use a phase-field order variable to represent interfaces. Natural fractures in geological materials have been represented by the phase-field variable that denotes the very state of the material damage assuming that the natural fractures have no cohesive strength [47, 67, 86]. The other approach is to represent interfaces by modifying their surface energy. Nguyen *et al.* proposed a model to account for interactions between interfacial damage and bulk fracture with micro-structural heterogeneities in

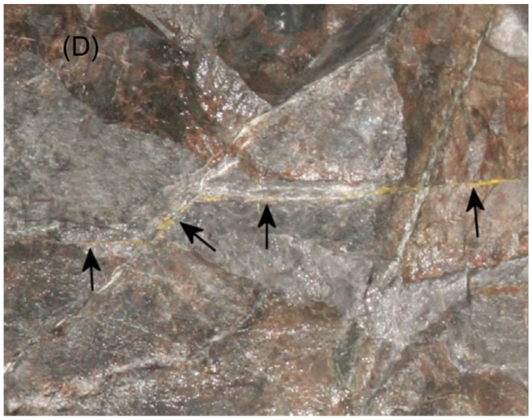

(a)

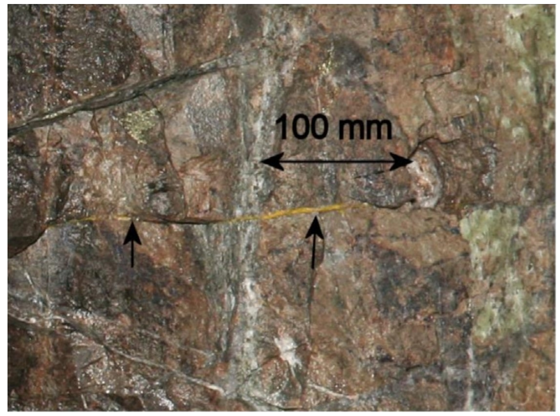

(b)

Figure 1: (a) Hydraulic fracture (marked by yellow proppant) offsetting while it crosses the natural fracture, and (b) hydraulic fracture interacts and crosses a mineralized fracture zone [44].

plaster and concrete [64, 65], and elastoplastic composites [52]. They combined the brittle phase-field approach for the bulk and the cohesive interface. The surface energy at the interfaces was then modified based on a level-set function and an additionally introduced phase-field order variable. This model was revisited by [69] for pre-existing adhesive interfaces in which the authors implemented a new interface finite element to map the jump discontinuity across the crack face instead of the level-set approach. Hansen–Dörr *et al.* proposed a non-invasive approach by assigning the modified fracture toughness over a diffused length to account for interfaces estimated from the surface energy equivalence [36, 37].

If an interface is represented by the phase-field variable, it will impact the stress and strain profiles around the interface and their profiles will depend on a choice of the strain energy decomposition [5, 31, 62, 75, 76]. On the other hand, altering the surface energy gives us a greater flexibility. It can represent interfaces that are weaker or stronger than the bulk depending on the assigned surface energy.

While the approaches proposed in [64, 65, 69] compare well with experimental observations, the implementation requires substantial changes in the existing phase-field formulation such as an additional phase-field variable or interface elements. On the contrary, the diffused interface approach proposed in [36, 37] is not implementation invasive and only requires to pre-compute the effective interface fracture toughness. However, the analytically derived effective interface fracture toughness in their studies underestimate the theoretical surface energy [36, 37], which need to be compensated by the empirical correction curves from a series of numerical simulations with various settings.

Our objective in this study is to derive an effective interface fracture toughness that does not require empirical compensation. We first revisit the formulation in [36, 37] considering the optimal phase-field profile and discretization effects. We then derive an effective interface fracture toughness that ensures the energy equivalence in closed form. The newly derived expression is verified to accurately reproduce the theoretical energy release rates in well known examples. The proposed approach is simple to use as it only needs to assign appropriate fracture toughness field and does not require changes in the formulation or use of special elements. Still, it can reproduce fracture impingement into an interface as predicted by the theory and effectively simulate hydraulic fracture interactions with natural fracture.

This paper is structured as follows. Section 2 shows the construction of the effective interface fracture toughness. We go through verification examples in Section 3. Section 4 highlights the capabilities in practical examples followed by conclusions in Section 5.

2. Construction of effective interface fracture toughness

2.1. Phase-field models for fracture

We consider a brittle-elastic medium $\Omega \subset \mathbb{R}^N$ with a crack set Γ (Fig. 2(a)). For the sake of simplicity, the body force and the external loading are considered absent. Then the potential energy is given as:

$$\mathcal{P} = \int_{\Omega\backslash\Gamma} W(\mathbf{u})\,\mathrm{d}\Omega, \tag{1}$$

where $W(\mathbf{u})$ is the strain energy density. Francfort and Marigo [29] recast Griffith's criterion as the minimization of the total energy, which is the sum of the potential and the fracture surface energy defined as:

$$\mathcal{F} := \mathcal{P} + \int_{\Gamma} G_\mathrm{c}\,\mathrm{d}\Gamma, \tag{2}$$

where G_c is the critical elastic energy release rate.

It is challenging to evaluate the crack surface energy for non-trivial crack geometry as it involves the surface integral over an evolving discrete crack set Γ. To overcome this challenge, the variational phase-field model proposed in [12] follows the approximation of [4] via Γ-convergence [16]. Introducing a scalar phase-field variable, $v : \Omega \mapsto [0, 1]$ and a regularization length parameter $\ell > 0$, the surface integral is approximated as:

$$\int_{\Gamma} G_\mathrm{c}\,\mathrm{d}\Gamma \approx \int_{\Omega} \frac{G_\mathrm{c}}{2}\left(\frac{(1-v)^2}{\ell} + \ell|\nabla v|^2\right)\mathrm{d}\Omega. \tag{3}$$

Alternatively, the phase-field model proposed in [62] is constructed from a geometrical approximation. Considering an infinite 1D bar $\mathcal{B} = [-\infty, +\infty] \times \Gamma$ with a crack at $x = 0$, the state of the material approximates the sharp fracture with the following profile:

$$v(x) = 1 - e^{-|x|/\ell}. \tag{4}$$

Accepting this profile, the followings are noticed:

1. (4) is the solution of the differential equation:

$$1 - v + \ell^2 v'' = 0, \text{ with } v(0) = 0 \text{ and } v(\pm\infty) = 1. \tag{5}$$

2. Then (5) is the Euler-Lagrange equation associated with the variational problem of:

$$J(v) := \frac{1}{2}\int_{-\infty}^{+\infty} \frac{(1-v)^2}{\ell} + \ell|v'|^2\,\mathrm{d}x.$$

This 1D analysis is extended to a multi-dimensional domain $\Omega \subset \mathbb{R}^N$ where the surface energy density function is approximated using the phase-field profile of (4):

$$S(v, \nabla v) := \frac{1}{2}\left(\frac{(1-v)^2}{\ell} + \ell|\nabla v|^2\right). \tag{6}$$

Using this density, the surface energy is approximated as:

$$\int_\Gamma G_\mathrm{c}\,\mathrm{d}\Gamma \approx G_\mathrm{c}\int_\Omega \frac{1}{2}\left(\frac{(1-v)^2}{\ell} + \ell|\nabla v|^2\right)\mathrm{d}\Omega. \tag{7}$$

The only difference between these two approaches amounts to the assumed profile of (4), which imposes the spatial uniformity on G_c. In other words, the profile of (4) is a special case when G_c is spatially uniform. We discuss the implications of this assumption in the next sub-section.

2.2. Interface model

To account for interfaces in phase-field models, [37] proposed to compute the effective interface fracture toughness $\tilde{G}_\mathrm{c}^\mathrm{int}$ diffused over a certain length b (Fig. 2(a)). The effective interface fracture toughness is assigned in this subdomain and the bulk toughness outside (Fig. 2(b)). The surface fracture energy dissipated at the interface is given as $G_\mathrm{c}^\mathrm{int}\int_\Gamma \mathrm{d}\Gamma$. Seeking the effective interface fracture toughness, we equate $G_\mathrm{c}^\mathrm{int}\int_\Gamma \mathrm{d}\Gamma$ to the approximated surface energy (3) using the diffused interface as:

$$G_\mathrm{c}^\mathrm{int}\int_\Gamma \mathrm{d}\Gamma = \tilde{G}_\mathrm{c}^\mathrm{int}\int_{\xi(\Gamma)<b} S(v, \nabla v)\,\mathrm{d}\Omega + G_\mathrm{c}^\mathrm{bulk}\int_{\xi(\Gamma)>b} S(v, \nabla v)\,\mathrm{d}\Omega, \tag{8}$$

where $\xi(\Gamma)$ is the shortest distance from the crack Γ. In the followings, we look into the two different approaches above to compute the effective interface fracture toughness in a 1D setting ($[0, +\infty] \times \Gamma$).

2.2.1. Phase-field approach

In [37], the energy equivalence in (8) was considered in the 1D setting. First, the surface energy expended at the interface is approximated as:

$$G_\mathrm{c}^\mathrm{int}\int_\Gamma \mathrm{d}\Gamma \approx G_\mathrm{c}^\mathrm{int}\int_0^\infty S(v, \nabla v)\,\mathrm{d}x \tag{9}$$

Using the profile of (4), (8) becomes

$$G_\mathrm{c}^\mathrm{int}\int_0^\infty \frac{e^{-2x/\ell}}{\ell}\,\mathrm{d}x = \tilde{G}_\mathrm{c}^\mathrm{int}\int_0^b \frac{e^{-2x/\ell}}{\ell}\,\mathrm{d}x + G_\mathrm{c}^\mathrm{bulk}\int_b^\infty \frac{e^{-2x/\ell}}{\ell}\,\mathrm{d}x. \tag{10}$$

Solving for $\tilde{G}_\mathrm{c}^\mathrm{int}$, we obtain[1]:

$$\tilde{G}_\mathrm{c}^\mathrm{int} = \frac{G_\mathrm{c}^\mathrm{int} - G_\mathrm{c}^\mathrm{bulk}e^{-2b/\ell}}{1 - e^{-2b/\ell}}. \tag{11}$$

As noted in [37], $\dfrac{2b}{\ell}$ must be greater than $\ln\dfrac{G_\mathrm{c}^\mathrm{bulk}}{G_\mathrm{c}^\mathrm{int}}$ so that $\tilde{G}_\mathrm{c}^\mathrm{int} > 0$.

[1] In the original notation in [37], $\ell = 2\ell_c$.

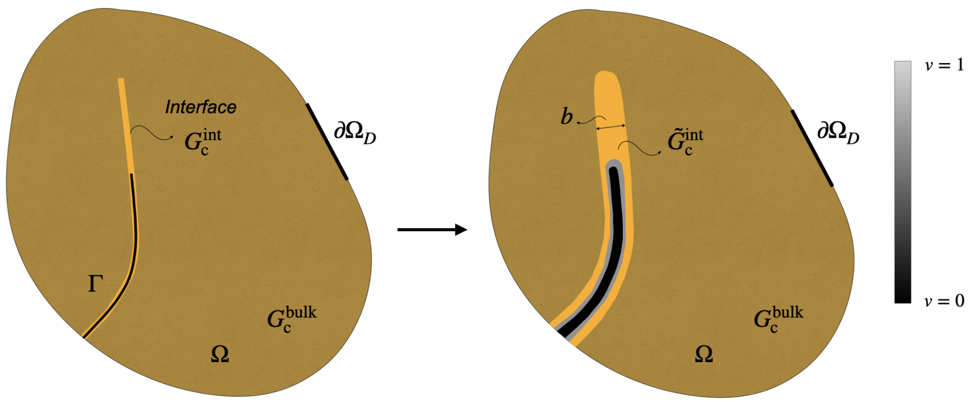

(a) Diffused representation of a discontinuous interface and a crack set Γ.

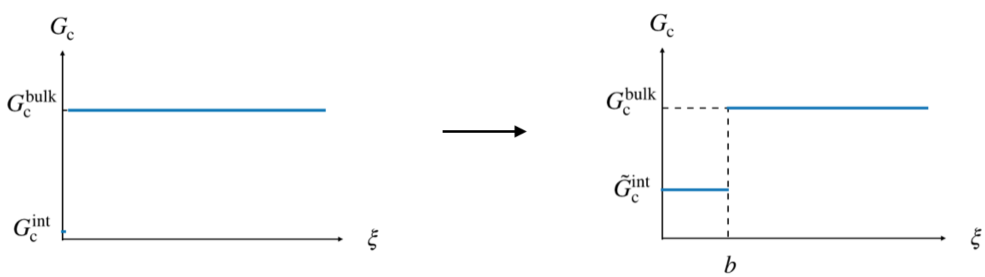

(b) Surface energy profile.

Figure 2: Diffused interface model: (a) schematic of diffused representation of a discontinuous and a crack set Γ, (b) Step-wise surface energy assigned over the subdomain $\xi < b$.

2.2.2. Variational approach

Here, we first construct the phase-field profile by seeking the optimal profile of v that minimizes (8) in the 1D setting:

$$\int_0^\infty G_\mathrm{c}(x)S(v,\nabla v)\,\mathrm{d}x := \int_0^\infty G_\mathrm{c}(x)\left(\frac{(1-v)^2}{\ell}+\ell|v'|^2\right)\mathrm{d}x \tag{12}$$

where

$$G_\mathrm{c}(x) = \begin{cases}\tilde{G}_\mathrm{c}^\mathrm{int} & \text{for } \; x<b,\\ G_\mathrm{c}^\mathrm{bulk} & \text{for } \; x>b.\end{cases} \tag{13}$$

If $G_\mathrm{c}(x)$ were uniform in x, (4) would be the optimal profile. The Euler-Lagrange equation in this case is:

$$\frac{\partial S_b}{\partial v} - \frac{\mathrm{d}}{\mathrm{d}x}\left(\frac{\partial S_b}{\partial v'}\right) = 0, \tag{14}$$

where $S_b := G_\mathrm{c}S$. Because of the discontinuity of $G_\mathrm{c}(x)$ at $x=b$, S_b depends on x. Thus, the Weierstrass-Erdmann corner conditions need to be ensured ([56], p. 167), which read:

$$\left.\frac{\partial S_b}{\partial v'}\right|_{x=b-0} = \left.\frac{\partial S_b}{\partial v'}\right|_{x=b+0}, \tag{15}$$

$$\left.\left(S_b - v'\frac{\partial S_b}{\partial v'}\right)\right|_{x=b-0} = \left.\left(S_b - v'\frac{\partial S_b}{\partial v'}\right)\right|_{x=b+0}. \tag{16}$$

Then the phase-field profile yields (see Appendix 6.1):

$$v = \begin{cases}1-\alpha_1 e^{-x/\ell} - (1-\alpha_1)e^{x/\ell} & \text{for } \; 0\le x\le b,\\ 1-\alpha_2 e^{-x/\ell} & \text{for } \; b\le x,\end{cases} \tag{17}$$

where

$$\begin{aligned}\alpha_1 &= \frac{(\tilde{G}_\mathrm{c}^\mathrm{int}+G_\mathrm{c}^\mathrm{bulk})e^{b/\ell}}{(\tilde{G}_\mathrm{c}^\mathrm{int}+G_\mathrm{c}^\mathrm{bulk})e^{b/\ell}+(\tilde{G}_\mathrm{c}^\mathrm{int}-G_\mathrm{c}^\mathrm{bulk})e^{-b/\ell}},\\ \alpha_2 &= \frac{2\tilde{G}_\mathrm{c}^\mathrm{int}e^{b/\ell}}{(\tilde{G}_\mathrm{c}^\mathrm{int}+G_\mathrm{c}^\mathrm{bulk})e^{b/\ell}+(\tilde{G}_\mathrm{c}^\mathrm{int}-G_\mathrm{c}^\mathrm{bulk})e^{-b/\ell}}.\end{aligned} \tag{18}$$

Remark 1. *The phase-field profile* (4) *proposed in [62] implicitly assumes a spatially uniform G_c. If G_c is not uniform in Ω, the optimal phase-field profile would differ such as in* (17)*.*

To compute $\tilde{G}_\mathrm{c}^\mathrm{int}$, we assume that the fracture surface energy at the interface can be approximated by (9). Using (5) and (17), we have

$$G_\mathrm{c}^\mathrm{int}\int_0^\infty \frac{2e^{-2x/\ell}}{\ell}\,\mathrm{d}x = \tilde{G}_\mathrm{c}^\mathrm{int}\int_0^b\left(\frac{(1-v)^2}{\ell}+\ell|v'|^2\right)\mathrm{d}x + G_\mathrm{c}^\mathrm{bulk}\int_b^\infty\left(\frac{(1-v)^2}{\ell}+\ell|v'|^2\right)\mathrm{d}x. \tag{19}$$

After performing the integrals, we arrive at

$$G_\mathrm{c}^\mathrm{int} = \tilde{G}_\mathrm{c}^\mathrm{int}\left\{\alpha_1^2\left(1-e^{-2b/\ell}\right) - \left(1-\alpha_1^2\right)\left(1-e^{2b/\ell}\right)\right\} + G_\mathrm{c}^\mathrm{bulk}\alpha_2^2 e^{-2b/\ell}. \tag{20}$$

(19) and (20) recover $G_\mathrm{c}^\mathrm{int} \to G_\mathrm{c}^\mathrm{bulk}$ and $\tilde{G}_\mathrm{c}^\mathrm{int} \to 0$ as $b \to 0$. Also, from (18) and (20), we have that $G_\mathrm{c}^\mathrm{int} \to \tilde{G}_\mathrm{c}^\mathrm{int}$ as $\ell \to 0$ or $b/\ell \to \infty$ (See Appendix 6.2). Fig. 3 compares $\tilde{G}_\mathrm{c}^\mathrm{int}$ from (20)[2] against (11). As reported in [37], $\tilde{G}_\mathrm{c}^\mathrm{int}$ computed from (11) underestimates the theoretical value.

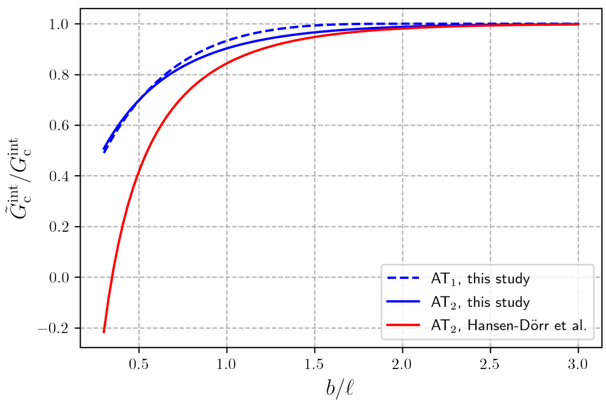

Figure 3: Comparison of 1D $\tilde{G}_\mathrm{c}^\mathrm{int}$ normalized by $G_\mathrm{c}^\mathrm{int}$ vs. b/ℓ. We set $G_\mathrm{c}^\mathrm{int}/G_\mathrm{c}^\mathrm{bulk} = 0.5$.

2.2.3. Variational approach - $\mathtt{AT}_1$ model

The approximated surface energy given in 3 is typically called the $\mathtt{AT}_2$ model as opposed to the $\mathtt{AT}_1$ model proposed more recently by [70]. Tanné *et al.* [79] performed thorough analyses comparing these two models in terms of crack nucleation and propagation. Their study found that the $\mathtt{AT}_1$ model, which posses an elastic phase prior to the failure, is superior over the $\mathtt{AT}_2$ model especially when there is no strong stress singularity. Given the increasing popularity of the $\mathtt{AT}_1$ model, here we expand our derivation of the effective interface toughness to the $\mathtt{AT}_1$ model.

The $\mathtt{AT}_1$ model approximates the surface energy as [15]:

$$\int_\Gamma G_\mathrm{c} \,\mathrm{d}\Gamma \approx \int_\Omega \frac{3G_\mathrm{c}}{8}\left(\frac{(1-v)}{\ell} + \ell|\nabla v|^2\right)\mathrm{d}\Omega. \tag{21}$$

For a constant G_c, the optimal phase-field profile is:

$$v = \begin{cases} 1 - \left(1 - \dfrac{|x|}{2\ell}\right)^2, & \text{for} \;\; |x| \le 2\ell \\ 1, & \text{for} \;\; |x| > 2\ell. \end{cases} \tag{22}$$

Unlike the $\mathtt{AT}_2$ model, the phase-field profile for $\mathtt{AT}_1$ has a finite transition length ($= 2\ell$). If we diffuse an interface beyond this transition length, then (8) ends up with $G_\mathrm{c}^\mathrm{int} = \tilde{G}_\mathrm{c}^\mathrm{int}$, which is equivalent to no interface. Therefore, we need to limit the diffused length b to be smaller than the

[2] As α_1 and α_2 contain $\tilde{G}_\mathrm{c}^\mathrm{int}$, solving (20) for $\tilde{G}_\mathrm{c}^\mathrm{int}$ requires an iterative root finding scheme such as `fsolve` function in python. The same goes for solving $\mathtt{AT}_1$ equivalence (27).

transition length 2ℓ in $\texttt{AT}_1$. With this constrain ($b < 2\ell$), similarly we can derive the optimal profile for the piecewise constant $G_c(x)$ in (13) as (see Appendix 6.1):

$$v = \begin{cases} -\dfrac{1}{4\ell^2}x^2 + \beta_1 x, & \text{for } \; 0 \leq x \leq b, \\ -\dfrac{1}{4\ell^2}x^2 + \beta_2 x + b(\beta_1 - \beta_2), & \text{for } \; b \leq x \leq 2\ell^2\beta_2, \\ 1, & \text{for } \; x \geq 2\ell^2\beta_2, \end{cases} \tag{23}$$

where

$$\beta_1 = \frac{G_c^{\text{bulk}}}{\tilde{G}_c^{\text{int}}}\left(-\frac{b}{2\ell^2} + \beta_2\right) + \frac{b}{2\ell^2}, \tag{24}$$

$$\beta_2 = \frac{1}{2\ell^2\tilde{G}_c^{\text{int}}}\left[-b\left(G_c^{\text{bulk}} - \tilde{G}_c^{\text{int}}\right) + G_c^{\text{bulk}}\sqrt{b^2 - \left(\frac{\tilde{G}_c^{\text{int}}}{G_c^{\text{bulk}}}\right)^2 b^2 + 4\left(\frac{\tilde{G}_c^{\text{int}}}{G_c^{\text{bulk}}}\right)^2 \ell^2}\,\right]. \tag{25}$$

Note that the transition length ($2\ell^2\beta_2$) is now dependent of the fracture toughness. Again, we equivalence the surface energies as:

$$G_c^{\text{int}} \int_0^{2\ell} \frac{2}{\ell}\left(1 - \frac{x}{2\ell}\right)^2 \mathrm{d}x$$
$$= \tilde{G}_c^{\text{int}} \int_0^{b} \left(\frac{(1-v)}{\ell} + \ell|v'|^2\right) \mathrm{d}x + G_c^{\text{bulk}} \int_b^{2\ell^2\beta_2} \left(\frac{(1-v)}{\ell} + \ell|v'|^2\right) \mathrm{d}x. \tag{26}$$

Then we obtain

$$\frac{4}{3}G_c^{\text{int}} = \tilde{G}_c^{\text{int}}\gamma_1 + G_c^{\text{bulk}}\gamma_2 \tag{27}$$

where

$$\gamma_1 = \frac{1}{6\ell^3}b^3 - \frac{\beta_1}{\ell}b^2 + \left(\ell\beta_1^2 + \frac{1}{\ell}\right)b, \tag{28}$$

$$\gamma_2 = -\frac{2}{3}\ell^3\beta_2^3 + 2\ell\beta_2 - 2\ell b\beta_2(\beta_1 - \beta_2) - \frac{b^3}{6\ell^3} + \frac{\beta_2 b^2}{\ell} - \left\{\ell\beta_2^2 + \frac{1}{\ell} - \frac{b}{\ell}(\beta_1 - \beta_2)\right\} b. \tag{29}$$

Similarly in $\texttt{AT}_1$, we recover $G_c^{\text{int}} \to G_c^{\text{bulk}}$ and $\tilde{G}_c^{\text{int}} \to 0$ as $b \to 0$. Since b is bounded by 2ℓ, the upper limit of b/ℓ is obtained as $b \to 2\ell$, $G_c^{\text{int}} \to \tilde{G}_c^{\text{int}}$ (See Appendix 6.2).

3. Verification examples

Although often neglected in phase-field analysis, the fracture toughness in simulation needs to account for the corresponding mesh discretization[3] relative to the theoretical value [13, 30, 87].

[3] The "numerical" toughness is given by $G_c(1 + h/2\ell)$ for $\texttt{AT}_2$ and $G_c(1 + 3h/8\ell)$ for $\texttt{AT}_1$ in phase-field models. Without accounting for this, the material toughness would vary with ℓ (h/ℓ to be precise). We refer to [13] (p. 103) or [87] for details.

Following this treatment, we consider the following numerical phase-field profile for $\mathtt{AT}_2$ for element discretization of size h in the 1D setting considered in (20)[4]:

$$v = \begin{cases} 0 & \text{for } \ x \leq h/2, \\ 1 - \alpha_1 e^{-(x-h/2)/\ell} - (1-\alpha_1) e^{(x-h/2)/\ell} & \text{for } \ h/2 < x < b' + h/2, \\ 1 - \alpha_2 e^{-(x-h/2)/\ell} & \text{for } \ b' + h/2 \leq x, \end{cases} \tag{30}$$

where $b' = b - h/2$. With this phase-field profile, (20) becomes

$$G_{\rm c}^{\rm int}\left(\frac{h}{2\ell}+1\right) = \tilde{G}_{\rm c}^{\rm int}\left\{\frac{h}{2\ell} + \alpha_1^2\left(1 - e^{-2b'/\ell}\right) - (1-\alpha_1)^2\left(1 - e^{2b'/\ell}\right)\right\} + G_{\rm c}^{\rm bulk}\alpha_2^2 e^{-2b'/\ell}. \tag{31}$$

Similarly, for $\mathtt{AT}_1$, the numerical phase-field profile is:

$$v = \begin{cases} 0 & \text{for } \ x \leq h/2, \\ -\dfrac{1}{4\ell^2}(x-h/2)^2 + \beta_1(x-h/2) & \text{for } \ h/2 \leq x \leq b' + h/2, \\ -\dfrac{1}{4\ell^2}(x-h/2)^2 + \beta_2(x-h/2) + b(\beta_1-\beta_2) & \text{for } \ b' + h/2 \leq x \leq 2\ell^2\beta_2 + h/2, \\ 1 & \text{for } \ x \geq 2\ell^2\beta_2 + h/2. \end{cases} \tag{32}$$

Then (27) becomes

$$G_{\rm c}^{\rm int}\left(\frac{h}{2\ell}+\frac{4}{3}\right) = \tilde{G}_{\rm c}^{\rm int}\left(\frac{h}{2\ell}+\gamma_1\right) + G_{\rm c}^{\rm bulk}\gamma_2. \tag{33}$$

Remark 2. *We recover* (20) *(resp.* (27)*) by setting* $h \to 0$ *in* (31) *(resp.* (33)*), but for a finite mesh size* h*, the numerical fracture toughness is dependent on* h *(or rather the ratio* h/ℓ*). Therefore, if the ratio* h/ℓ *varies in the domain, so does the numerical fracture toughness.*

In the following verification examples, we compute the effective interface fracture toughness $\tilde{G}_{\rm c}^{\rm int}$ using (31) for $\mathtt{AT}_2$ and (33) for $\mathtt{AT}_1$. We refer to Appendix 6.3 for detailed implementation of the model.

3.1. Surfing boundary example

We first verified the phase-field profile under non-uniform $G_{\rm c}$ in (17) using the surfing example [41]. Consider a computational domain, $\Omega = [0, L] \times [-H/2, H/2]$ with an edge crack, $\Gamma = [0, a_0] \times \{0\}$, and a diffused interface $[0, L] \times [-b, b]$ (Fig. 4(a)) which is subjected to a time dependent crack opening displacement:

$$\mathbf{u}(x, y, t) = \mathbf{U}(x - \mathrm{v}t, y) \quad \text{on} \quad \partial\Omega_D, \tag{34}$$

where v is an imposed loading velocity; and $\mathbf{U}$ is the asymptotic solution for the Mode-I crack opening displacement

$$\begin{aligned} U_x &= \frac{K_I}{2\mu}\sqrt{\frac{r}{2\pi}}(\kappa - \cos\varphi)\cos\frac{\varphi}{2}, \\ U_y &= \frac{K_I}{2\mu}\sqrt{\frac{r}{2\pi}}(\kappa - \cos\varphi)\sin\frac{\varphi}{2}, \end{aligned} \tag{35}$$

[4] We consider a crack is represented by $v = 0$ in an entire element rather than by a node because, in simulation, a crack propagates through elements not the element boundaries (*i.e.*, nodes).

where K_I is the stress intensity factor, $\kappa = (3-\nu)/(1+\nu)$ and $\mu = E/2(1+\nu)$; (r, φ) are the polar coordinate system, where the origin is crack tip. Also, we used $G_c^{\text{int}} = K_{Ic}^2(1-\nu^2)/E$ as the fracture surface energy under plane strain condition. Table 1 lists the material properties and geometry of the numerical model. The domain was meshed with uniform quadrilateral elements to avoid varying h/ℓ.

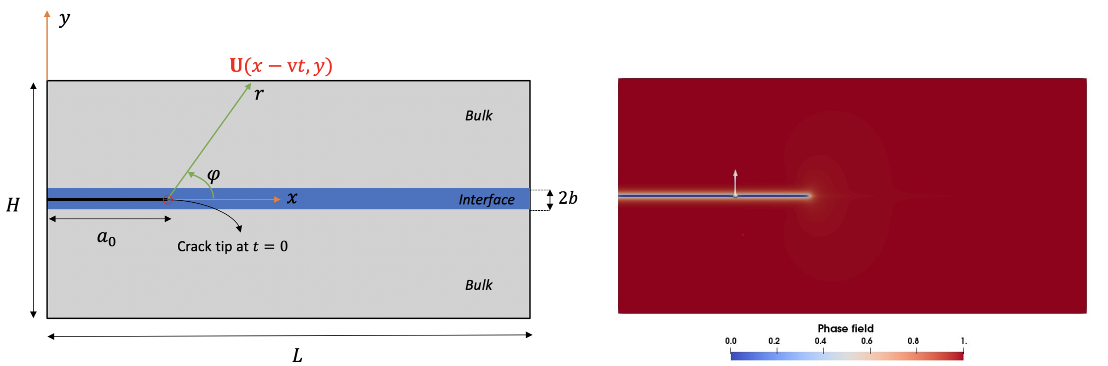

(a) (b)

Figure 4: (a) Schematic view of surfing boundary condition benchmark where an interface exists. Geometry and boundary conditions. (b) Phase-field profiles obtained from varying G_c at $t = 0.2t_f$. We set $l = 2h$, and $b/\ell = 0.75$. The white arrow, $\{0.5\} \times [0, 0.1]$, illustrates the line where we plot the phase-field profile in Fig. 5.

Table 1: Phase-field profile and surfing boundary example: Material properties [37] and geometrical parameters.

Name	Symbol	Value	Unit
Young's modulus	E	210×10^3	MPa
Critical energy release rate of bulk	G_c^{bulk}	5.4	MPa·mm
Critical energy release rate of interface	G_c^{int}	2.7	MPa·mm
Poisson's ratio	ν	0.3	–
Effective element size	h	5×10^{-3}	mm
Regularization parameter	ℓ	1×10^{-2}	mm
Imposed loading velocity	v	1.5	mm/s
Length	L	2	mm
Height	H	1	mm
Initial crack length	a_0	0.5	mm

Simulated phase-field profiles were taken along the orthogonal line indicated in Fig. 4(b) and match closely with (30) (Fig. 5) for $\texttt{AT}_2$ and with (32) (Fig. 6) for $\texttt{AT}_1$. The profiles exhibit a kink at $\xi = b$ and deviate from the well known exponential form (4) for $\texttt{AT}_2$ and from the quadratic form (22) for $\texttt{AT}_1$ more profoundly with smaller b/ℓ.

We computed the energy release rate using G_θ method [27, 53] with various b/ℓ ratios and plot the errors against the theoretical numerical toughness *i.e.* $(G_c)_{\text{num}} = G_c(1 + h/2\ell)$ for $\texttt{AT}_2$ and $(G_c)_{\text{num}} = G_c(1 + 3h/8\ell)$ for $\texttt{AT}_1$ [13, 87] in Fig. 7. The effective interface fracture toughness $\tilde{G}_c^{\text{int}}$ computed from (31) with various h/ℓ ratios are in an excellent agreement with the theoretical

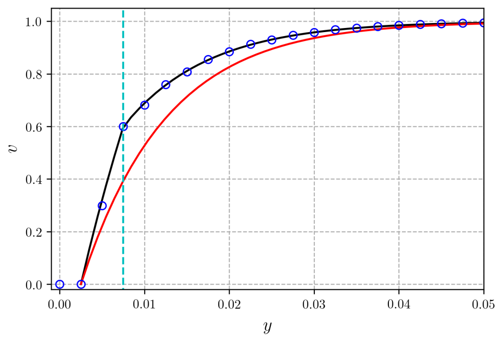

(a) $b/\ell = 0.75$

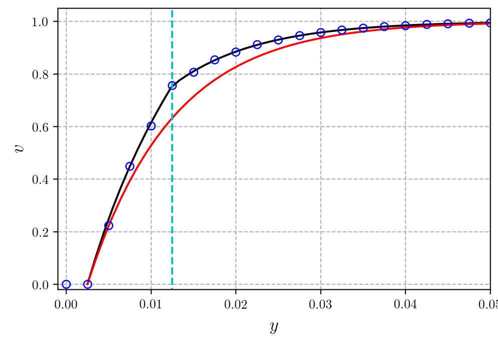

(b) $b/\ell = 1.25$

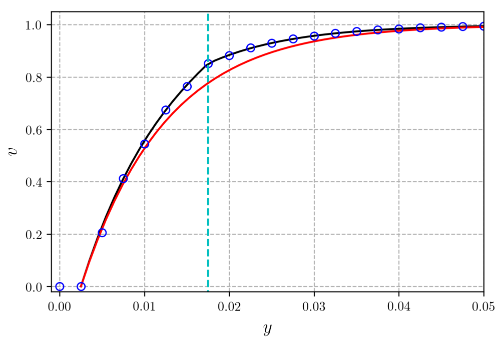

(c) $b/\ell = 1.75$

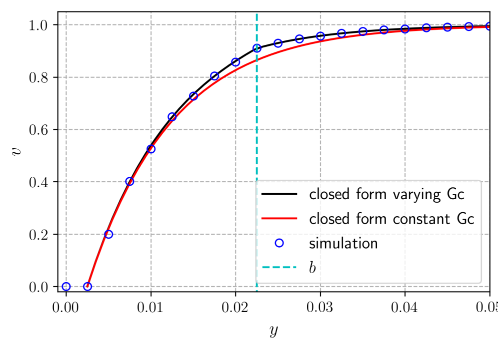

(d) $b/\ell = 2.25$

Figure 5: Phase-field profiles obtained from varying G_c in $\texttt{AT}_2$. We set $l = 2h$ and plot the phase-field profile over $\{0.5\} \times [0, 0.1]$, at $t = 0.2t_f$. The slope of the phase-field profile at $y = b$ changes due to the discontinuities of G_c at interface.

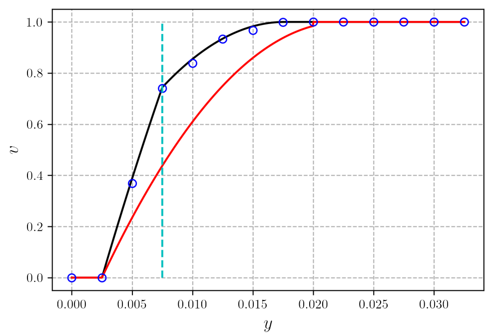

(a) $b/\ell = 0.75$

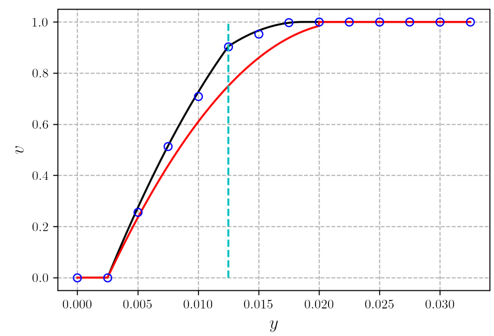

(b) $b/\ell = 1.25$

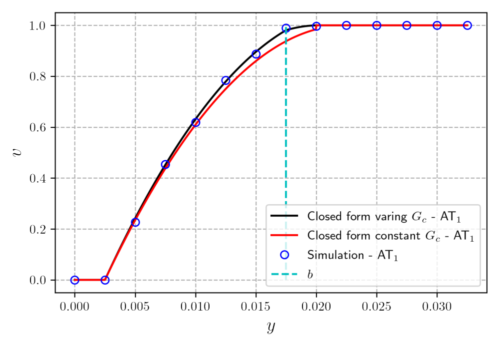

(c) $b/\ell = 1.75$

Figure 6: Phase-field profiles obtained from varying G_c in $\texttt{AT}_1$. We set $l = 2h$ and plot the phase-field profile over $\{0.5\} \times [0, 0.03]$, at $t = 0.2t_f$. The slope of the phase-field profile at $y = b$ changes due to the discontinuities of G_c at interface.

critical energy release rates despite the 1D consideration in its construction. In all the settings, the errors are within 2% and even less for $\mathtt{AT}_1$ (Fig. 7).

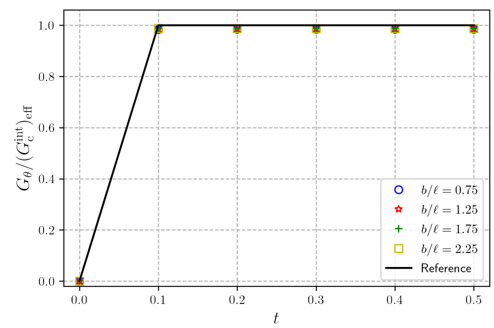

(a) G_θ comparison $\mathtt{AT}_2$

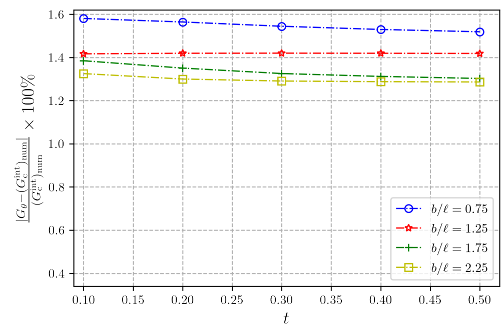

(b) G_θ relative error $\mathtt{AT}_2$

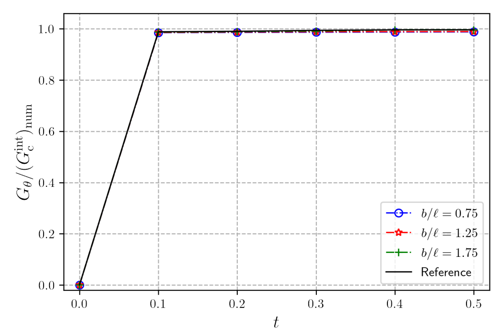

(c) G_θ comparison $\mathtt{AT}_1$

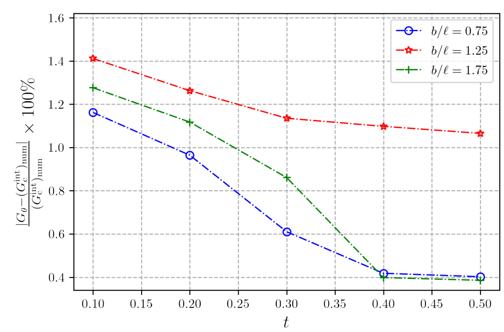

(d) G_θ relative error $\mathtt{AT}_1$

Figure 7: The computed energy release rate vs. time under plane strain condition. We used virtual perturbation of θ to compute energy release rate using G_θ [27]. The θ value is 1 inside of $B_r(P)$, 0 outside, and a linear interpolation in between. We set $r = 4\ell$ and $R = 2.5r$ (see [54]).

3.2. Sneddon's problem - 2D

We verified the model with plane-strain hydraulic fracture propagation in a toughness dominated regime based on Sneddon's solution [74], a widely used verification example in hydraulic fracturing simulation [11, 25, 32, 34, 45, 48, 63]. The problem was solved in an infinite 2D domain with a line crack $[-a_0, a_0] \times \{0\}$. To account for the infinite boundaries in the closed-form solution, a finite domain $[-L/2, L/2] \times [-L/2, L/2]$ with a diffused interface $[-L/2, L/2] \times [-b, b]$ (Fig. 8) was embedded in a larger domain $[-5L, 5L] \times [-5L, 5L]$ in the computations. The sub-domain $[-L/2, L/2] \times [-L/2, L/2]$ was meshed with uniform quadrilateral elements to ensure invariant h/ℓ.

The critical volume for crack propagation is given as $V_c := \sqrt{\dfrac{4\pi G_c a_0^3}{E'}}$ and the corresponding

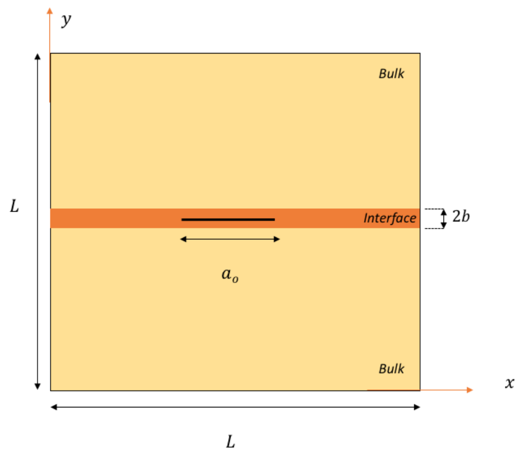

Figure 8: Schematic view of Sneddon's problem with a finite strip of compensated interface.

pressure and the crack length evolutions are given as follows:

$$p(V) = \begin{cases} \dfrac{E'V}{2\pi a_0^2} & V < V_c \\ \left[\dfrac{2E'G_{\mathrm{c}}^2}{\pi V}\right]^{\frac{1}{3}} & V \geq V_c, \end{cases} \tag{36}$$

$$a(V) = \begin{cases} a_0 & V < V_c \\ \left[\dfrac{2E'V^2}{4\pi G_{\mathrm{c}}}\right]^{\frac{1}{3}} & V \geq V_c. \end{cases} \tag{37}$$

To account for the hydraulic force on the crack lips, we need to add the work done by the fluid pressure to the total energy. We refer to Appendix 6.4 for this extension. Taking advantage of the linearity of the system, the simulations were run with the dimensionless properties listed in Table 2.

Table 2: Parameter values for the Sneddon benchmark.

Name	Symbol	Value
Young's modulus	E	1.0
Critical energy release rate of bulk	$G_{\mathrm{c}}^{\mathrm{bulk}}$	2.0
Critical energy release rate of interface	$G_{\mathrm{c}}^{\mathrm{int}}$	1.0
Poisson's ratio	ν	0.15
Effective element size	h	1×10^{-3}
Regularization parameter	ℓ	2×10^{-3}
Length	L	0.6
Initial crack length	a_0	0.1

From (19) and (26), we can retrieve the crack length a as:

$$a = \frac{\displaystyle\int_\Omega \frac{G_{\mathrm{c}}}{4c_n}\left(\frac{(1-v)^n}{\ell} + \ell|\nabla v|^2\right) \mathrm{d}\Omega}{G_{\mathrm{c}}^{\mathrm{int}}\left(\dfrac{h}{4c_n\ell} + 1\right)}. \tag{38}$$

where $n = 1$ corresponds to $\mathtt{AT}_1$ ($c_n = 1/2$) and $n = 2$ to $\mathtt{AT}_2$ ($c_n = 2/3$). Computed pressures and retrieved crack lengths are in a close agreement with the closed form solutions (Fig. 9).

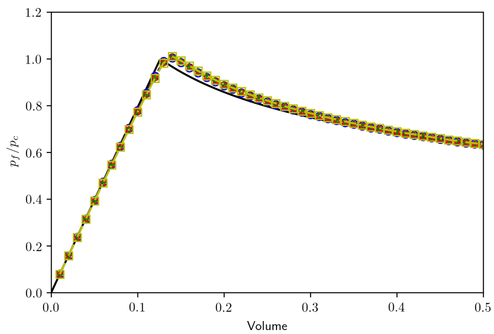

(a) Fracture pressure $\mathtt{AT}_2$

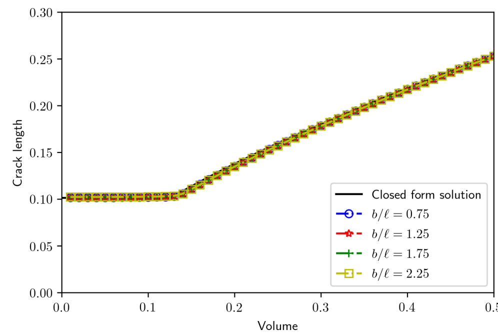

(b) Fracture length $\mathtt{AT}_2$

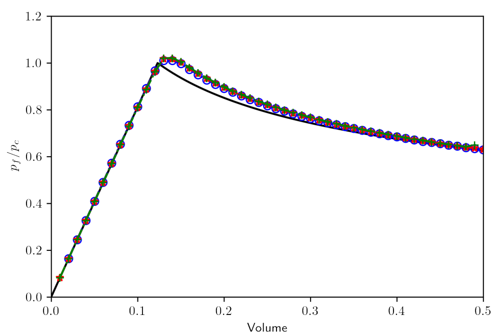

(c) Fracture pressure $\mathtt{AT}_1$

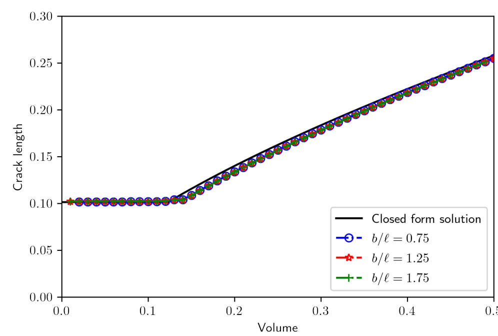

(d) Fracture length $\mathtt{AT}_1$

Figure 9: Comparison of the fracture pressure (a, c) and the length (b, d) against the closed form solution.

3.3. Sneddon's problem - 3D

As our last verification example, we applied our approach to penny-shape hydraulic fracturing in 3D. The analytical solution is developed in an infinite 3D domain with a circular crack $[0, a_0] \times [0, 2\pi]$ in the polar coordinate. All the parameters are the same as the 2D example except that we ran only the $\mathtt{AT}_1$ model and the mesh size is $h = 2.5 \times 10^{-3}$.

Applying the symmetry, we extruded the 2D mesh only in the positive z-direction by $5h$ with the same resolution and then by 0.5 with a 10 times coarser ($10h$) resolution (Figure 10(a)). The reason for this first extrusion of $5h$ is that the $\texttt{AT}_1$ model has a finite support ($2\ell = 4h$) and its numerical fracture toughness is not impacted by varying h/ℓ beyond this length.

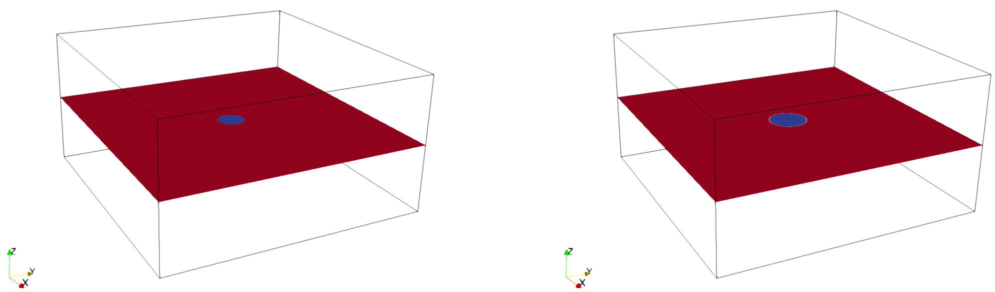

(a) Initial penny-shape crack.

(b) Penny-shape crack growth in 3D.

Figure 10: Sneddon's problem in 3D: (a) Initial penny-shape crack. (b) Penny-shape crack growth at $V = 0.37V_c$.

Using Sneddon's closed form solution [74], we obtain the critical volume as $V_c := \frac{8}{3}\sqrt{\frac{\pi G_c a_0^5}{E'}}$ and the following pressure and crack length evolutions [78]:

$$p(V) = \begin{cases} \dfrac{3E'V}{16\pi a_0^3} & V < V_c \\ \left[\dfrac{\pi^3 E'^2 G_\mathrm{c}^3}{12V}\right]^{\frac{1}{5}} & V \geq V_c, \end{cases} \tag{39}$$

$$a(V) = \begin{cases} a_0 & V < V_c \\ \left[\dfrac{9E'V^2}{64\pi G_\mathrm{c}}\right]^{\frac{1}{5}} & V \geq V_c. \end{cases} \tag{40}$$

Note that the crack radius can be recovered from:

$$r = \left[\frac{\displaystyle\int_\Omega \frac{G_\mathrm{c}}{4c_n}\left(\frac{(1-v)^n}{\ell} + \ell|\nabla v|^2\right)\mathrm{d}\Omega}{G_\mathrm{c}^{\mathrm{int}}\left(\dfrac{h}{4c_n\ell}+1\right)\pi}\right]^{1/2}. \tag{41}$$

Figure 10(b) shows a simulated penny-shape crack at $V = 0.37V_c$. Computed pressures and crack radii are plotted against the closed form solution in Figure 11. The agreements are not as close as the 2D examples. This is because of the coarser element size used (2.5 times bigger) in the 3D examples for tractable computational time[5].

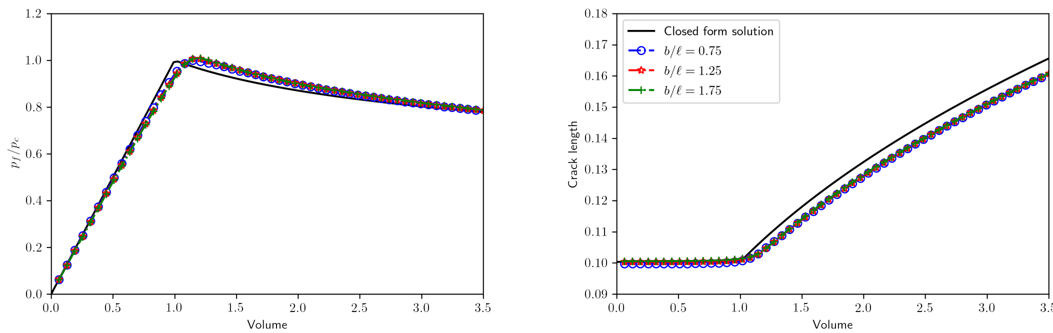

(a) Fracture pressure $\mathtt{AT}_1$

(b) Fracture radius $\mathtt{AT}_1$

Figure 11: Comparison of the fracture pressure (a) and the radius (b) against the closed form solution.

4. Numerical examples

This section demonstrates the capabilities of the model through examples where a weak interface is located away from an initial crack with some inclination. In such configurations, an interface ahead of the propagating fracture experiences compressional loading. Therefore, the strain energy in (65) needs to be decomposed depending on the state of the strain as originally pointed out by [5]. In the following examples, we employed the approach proposed by Miehe *et al.* [62] based on a spectral decomposition of the strain.

4.1. Static crack impinging on an interface

This example aims to investigate the competition between deflection and penetration of a crack that impinges into an interface. Consider a computational domain, $\Omega = [0, L] \times [-H/2, H/2]$, with an edge crack $\Gamma = [0, a_0] \times \{0\}$ and an interface with an inclined angle, β under plane strain condition (Fig. 12). The materials are homogeneous on either side of the interface. The specimen has the edge length $L = 2$ and $H = 1.8$. We set $b = 1.25\ell$. Also, the computational domain is subjected to the surfing boundary conditions (Section 3.1). The remaining input data can be found in Table 1.

He and Hutchinson *et al.* [38, 42] have studied a crack that impinges on an interface joining bi-material that is subjected to remote static loading. For the homogeneous case, the ratio of the mode-I static crack energy release rate ($\mathcal{G}_{\mathrm{I}}$) and the deflected crack tip ($\mathcal{G}^{\mathrm{int}}$) is a function of interfacial angle, β [6, 83]:

[5]The total number of nodes is 5,621,772. The simulations were distributed to 960 cores over 20 nodes with 2×24 cores. The computational times were between 20 to 24 hours in the 3D examples.

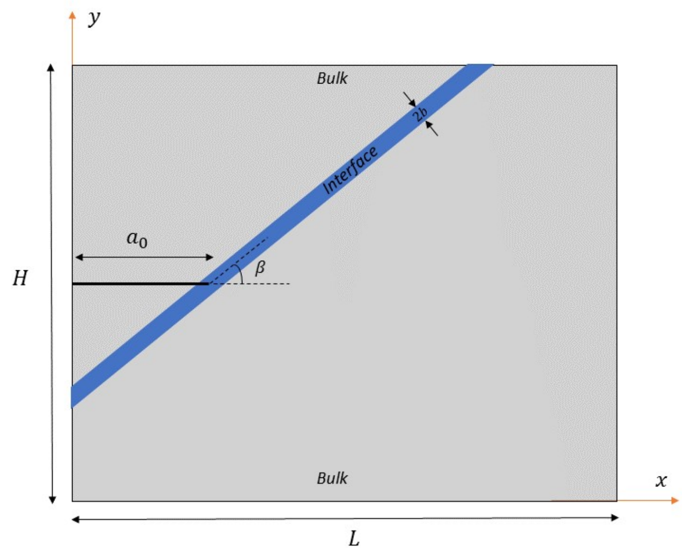

Figure 12: Schematic view of crack impinging on an interface.

$$\frac{\mathcal{G}^{\text{int}}}{\mathcal{G}_{\text{I}}} = \frac{1}{16}\left[\left(3\cos\frac{\beta}{2} + \cos\frac{3\beta}{2}\right)^2 + \left(\sin\frac{\beta}{2} + \sin\frac{3\beta}{2}\right)^2\right]. \tag{42}$$

For a deflecting crack at an interface, we consider the maximum energy release rate criterion which is to find a propagation angle θ that maximizes the energy release rate [19, 50]:

$$\max_{\theta\in[0,2\pi)} \frac{\mathcal{G}(\theta)}{G_{\text{c}}(\theta)}. \tag{43}$$

Using (42) and (43), the condition for crack penetration into the bulk is given as:

$$\frac{\mathcal{G}^{\text{int}}}{\mathcal{G}_{\text{I}}} < \frac{G_{\text{c}}^{\text{int}}}{G_{\text{c}}^{\text{bulk}}}. \tag{44}$$

Otherwise it deflects into the interface [38, 42]. As predicted by this criterion, the crack deflects into the interface for $\frac{\mathcal{G}^{\text{int}}}{\mathcal{G}_{\text{I}}} > \frac{G_{\text{c}}^{\text{int}}}{G_{\text{c}}^{\text{bulk}}}$ while the crack penetrates into the bulk for $\frac{\mathcal{G}^{\text{int}}}{\mathcal{G}_{\text{I}}} < \frac{G_{\text{c}}^{\text{int}}}{G_{\text{c}}^{\text{bulk}}}$ (Fig. 13). Both $\texttt{AT}_1$ and $\texttt{AT}_2$ results depict the identical deflection/penetration behaviors.

4.2. Hydraulic fracturing with a natural fracture

In this example, we simulated hydraulic fracture interactions with a pre-existing natural fracture which has a weaker toughness (partially cemented) than the bulk material, using the $\texttt{AT}_2$ model. Consider a natural fracture with a length of $l = 0.2$ placed $a_0/2$ away from the initial fracture with an inclination angle of α in the same setting as in Fig. 8 except that $a_0 = 0.05$ (Fig. 14). We consider

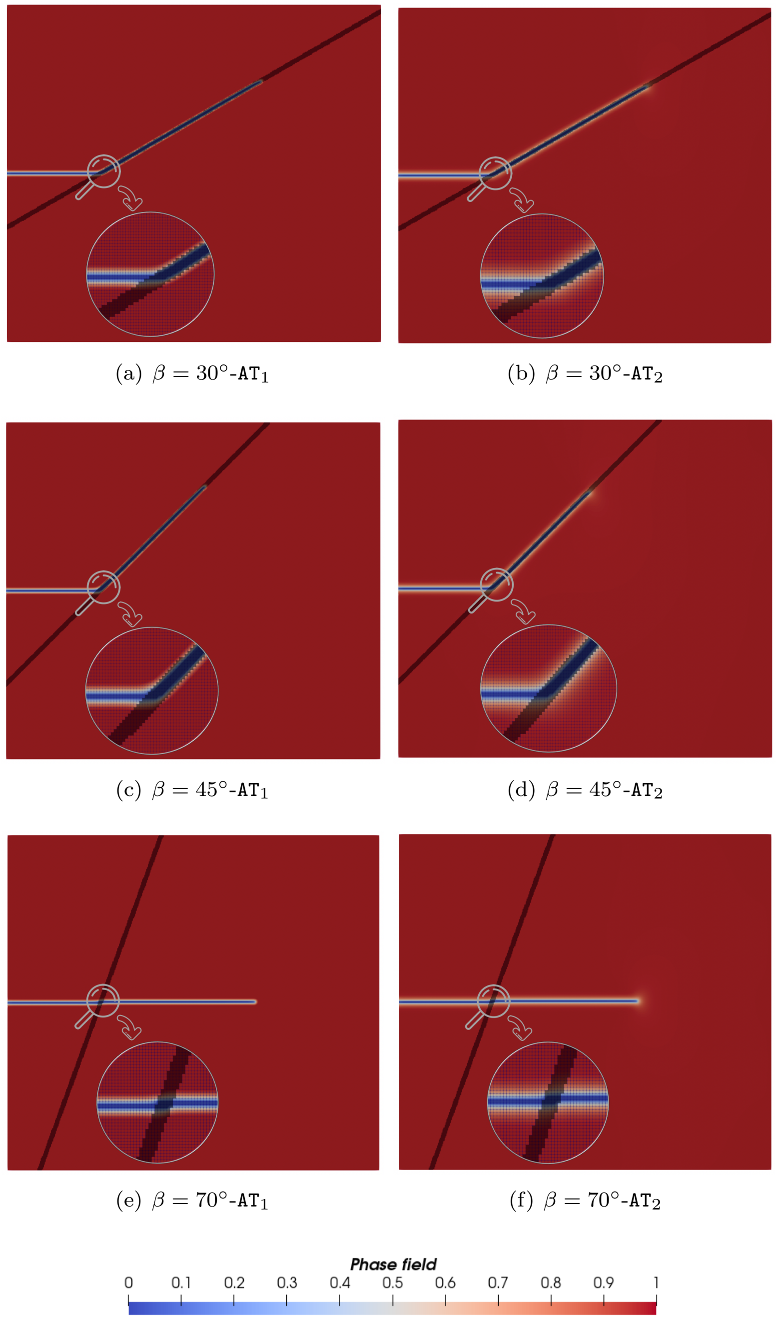

(a) $\beta = 30°$-$\mathtt{AT}_1$

(b) $\beta = 30°$-$\mathtt{AT}_2$

(c) $\beta = 45°$-$\mathtt{AT}_1$

(d) $\beta = 45°$-$\mathtt{AT}_2$

(e) $\beta = 70°$-$\mathtt{AT}_1$

(f) $\beta = 70°$-$\mathtt{AT}_2$

Figure 13: Phase-field profile for crack impinging on an interface with different interfacial angle, β. (a) - (d) show the crack deflecting into the interface $\left(\frac{\mathcal{G}^{\text{int}}}{\mathcal{G}_{\text{I}}} \geq \frac{G_{\text{c}}^{\text{int}}}{G_{\text{c}}}\right)$, while (e) and (f) show that the crack penetrating into the bulk $\left(\frac{\mathcal{G}^{\text{int}}}{\mathcal{G}_{\text{I}}} < \frac{G_{\text{c}}^{\text{int}}}{G_{\text{c}}}\right)$. The black line indicates the interface.

two different angles, $\alpha = 90°$ and $165°$, and two different interface toughness of $G_c^{int}/G_c^{bulk} = 0.2$ and 0.5, which imply that the natural fractures respectively have 20% and 50% of the bulk fracture toughness. The other material properties are the same as in Section 3.3.

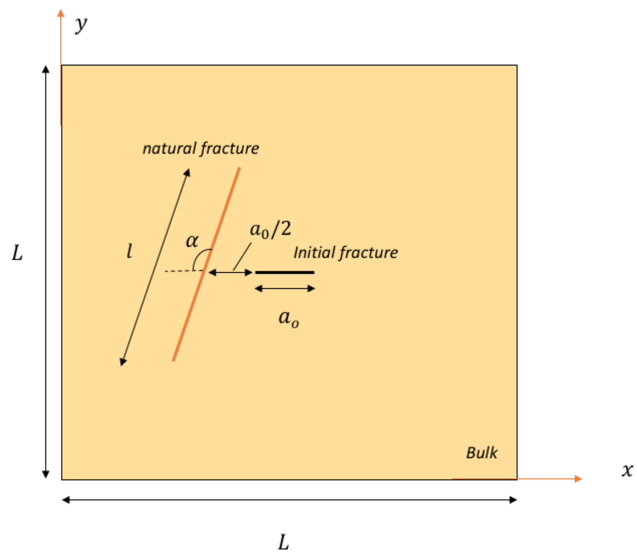

Figure 14: Schematic view of hydraulic fracturing with a natural fracture.

Fig. 15 shows hydraulic fracture profiles at the initial condition, and at the injection volume of 0.35 ($V = 0.35$) for $G_c^{int}/G_c^{bulk} = 0.2$ and 0.5 with $\alpha = 90°$. The hydraulic fracture in the $G_c^{int}/G_c^{bulk} = 0.2$ case (Fig. 15(b)) branches into two fractures. On the contrary, for the $G_c^{int}/G_c^{bulk} = 0.5$ case (Fig. 15(c)), the hydraulic fracture does not "see" the natural fracture and keeps propagating in the original direction.

With $\alpha = 165°$, the natural fracture impacts the hydraulic fracture paths significantly and changes the direction for both $G_c^{int}/G_c^{bulk} = 0.2$ and 0.5 cases (Fig. 16). Even though the hydraulic fractures end up along the natural fracture in both cases, a careful observation can reveal that the inflection angles towards the natural fracture are slightly different. The smaller G_c^{int}/G_c^{bulk}, the earlier the hydraulic fracture is attracted to the natural fracture (Figs. 16(b) and 16(c)). This attraction towards the weak interface is possibly due to both numerics and physics. With the smeared representation of crack, the crack tip can "feel" the presence of interfaces a little earlier than the sharp representation counterpart. At the same time, as the crack approaches, the weaker interface can start forming damage before the bulk material and thus can deform more, which attracts the crack tip.

The question in practice would be whether we see any signatures on the pressure response [49, 68]. Turning our attention to the pressure responses, we see that in all the cases, the pressure first builds up to the critical value and declines as the fracture grows (Fig. 17).

Though the natural fracture does not seem to impact the hydraulic fracture propagation path for the $\alpha = 90°$ and $G_c^{int}/G_c^{bulk} = 0.5$ case (Fig. 15(c)), the pressure drops slightly when the hydraulic fracture crosses the natural fracture (Fig. 17(a)). In other three cases, the pressures drop substantially when the hydraulic fracture turns into the natural fracture, which agrees with

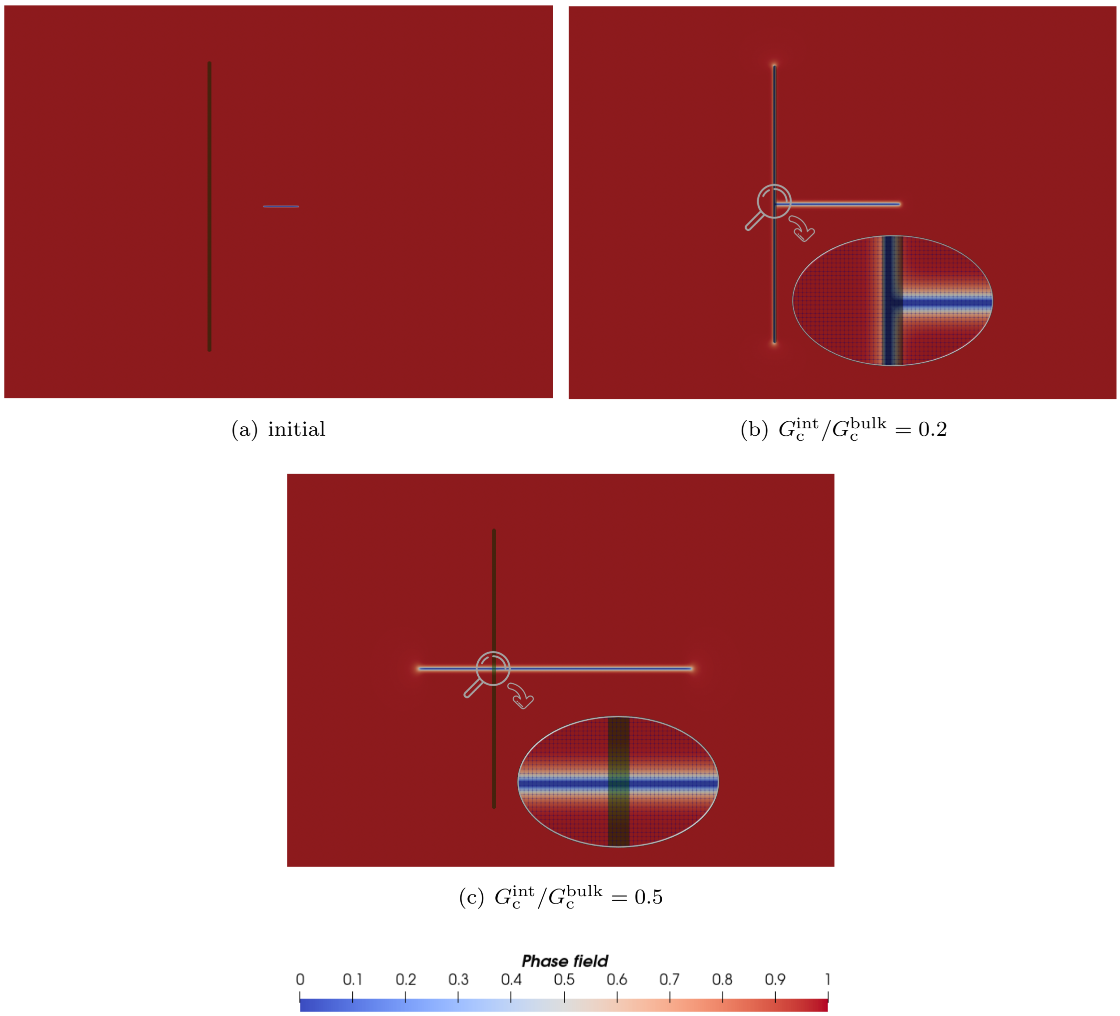

(a) initial

(b) $G_c^{\text{int}}/G_c^{\text{bulk}} = 0.2$

(c) $G_c^{\text{int}}/G_c^{\text{bulk}} = 0.5$

Figure 15: Phase-field profile for hydraulic fracturing interacting with a natural fracture: (a) the initial crack is represented by the phase-field and the physical location of the natural fracture with $\alpha = 90^\circ$ is indicated by the black line, (b) shows the $G_c^{\text{int}}/G_c^{\text{bulk}} = 0.2$ case with fracture propagation along the natural fracture and (c) shows the $G_c^{\text{int}}/G_c^{\text{bulk}} = 0.5$ case where the hydraulic fracture bypassed the natural fracture.

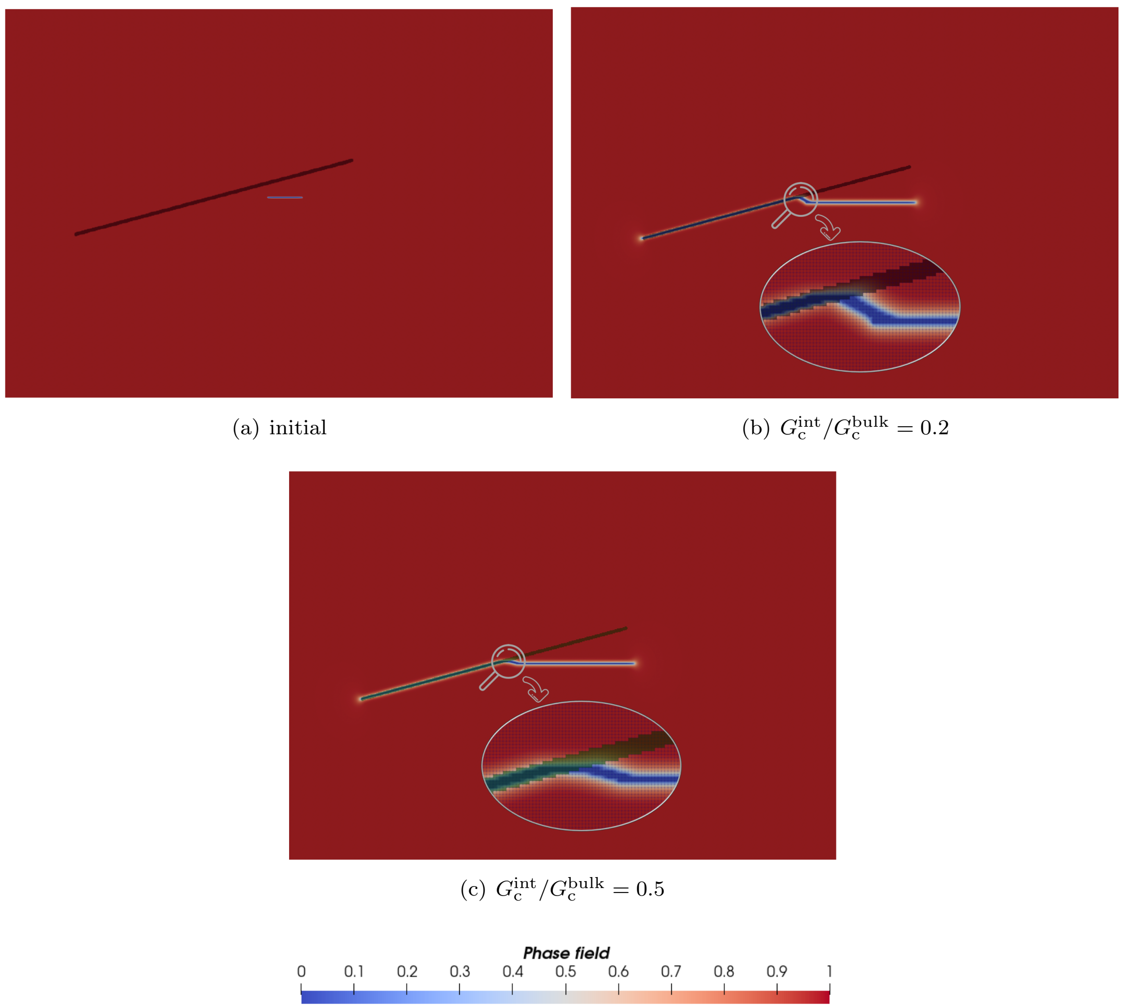

(a) initial

(b) $G_c^{\text{int}}/G_c^{\text{bulk}} = 0.2$

(c) $G_c^{\text{int}}/G_c^{\text{bulk}} = 0.5$

Figure 16: Phase-field profile for hydraulic fracturing interacting with a natural fracture: (a) the initial crack is represented by the phase-field and the physical location of the natural fracture with $\alpha = 165°$ is indicated by the black line, (b) shows a $G_c^{\text{int}}/G_c^{\text{bulk}} = 0.2$ and (c) the $G_c^{\text{int}}/G_c^{\text{bulk}} = 0.2$ case. Both cases show the hydraulic fracture turning into the natural fracture but with different angles.

experimental observations [55, 60]. Once the fracture tip is out of the natural fracture, the higher pressure is required to fracture the bulk rock.

One distinguished response is the double dip in the case for $\alpha = 90°$ and $G_c^{\text{int}}/G_c^{\text{bulk}} = 0.2$ (Fig. 17(a)). The first small drop occurs immediately before the hydraulic fracture hits the natural fracture, then the second when branching preceded by a small build up.

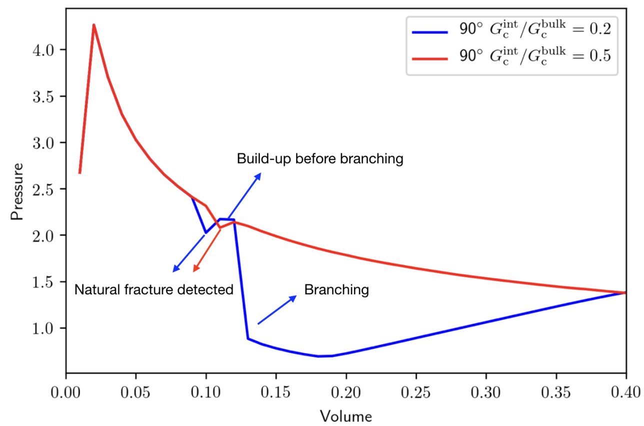

(a) $\alpha = 90°$

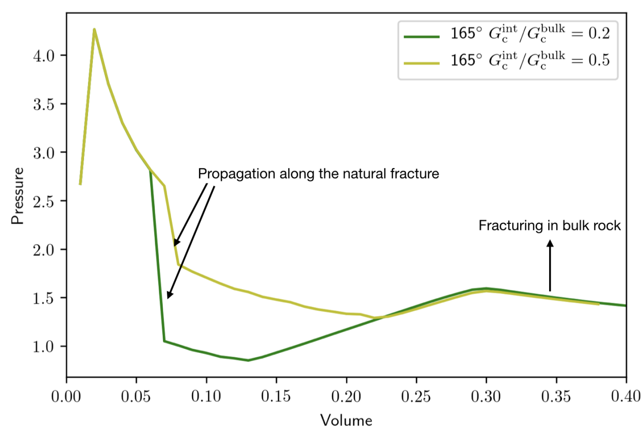

(b) $\alpha = 165°$

Figure 17: Pressure responses from all four cases of Section 4.2.

5. Conclusion

In this study, we proposed an approach to approximate the effective interface fracture toughness for a diffused interface by equating the diffused surface energy to the sharp representation. In deriving the effective interface fracture toughness, we demonstrated that the widely accepted exponential phase-field profile ($\mathtt{AT}_2$) applies only for a spatially uniform fracture toughness and the optimal phase-field profile takes a different form otherwise. The optimal phase-field profile needs to meet the Weierstrass-Erdmann conditions at the discontinuity for a spatially varying fracture toughness considered in this study.

Our approach to model the interface is very simple compared to previously proposed methods because:

1. the effective interface fracture toughness is computed from a closed-form equation without the need of running extra simulations and
2. it does not require any changes in the existing phase-field implementation.

Despite its simplicity, the approach accurately reproduced the critical energy release rates in two well known examples.

As our final remarks, we note two possible future studies.

1. If a crack propagates towards a *stronger* interface, the maximum energy release rate criterion [19, 50] will *exclude* the propagation along the interface. Quantitative investigation of energy expenditures may be needed in such scenarios.
2. Hydraulic fracture interaction with natural fractures have been studied experimentally [43, 60], analytically [22] and numerically [24, 59, 80, 82]. Although some semi-analytical criteria have been proposed in [33, 88], further studies may be needed to establish a unified criterion that includes the interface (natural fracture) toughness and behaviors of kinking and branching as observed in this study.

CRediT authorship contribution statement

Keita Yoshioka: Conceptualization, Methodology, Software, Validation, Formal analysis, Writing - original draft, Visualization, Funding acquisition. **Mostafa Mollaali:** Validation, Formal analysis, Writing - review & editing, Visualization. **Olaf Kolditz:** Funding acquisition.

Acknowledgements

The authors gratefully acknowledge the funding provided by the German Federal Ministry of Education and Research (BMBF) for the GeomInt project (Grant Number 03G0866A), by BMBF (grant number 02NUK053E) and Helmholtz Association (grant number SO-093) for the iCROSS-Project, and by EURAD, the European Joint Programme on Radioactive Waste Management for DONUT (Grant Agreement No 847593). Some simulations were run on the computation time provided through the Earth System Modeling Project (ESM) partition of the supercomputer JUWELS at the Jülich Supercomputing Centre (JSC).

The first author (KY) would like to express his deepest gratitude to Dr. Jose Adachi and Dr. Blaise Bourdin for their careful review of the manuscript and invaluable feedback.

6. Appendix

6.1. Optimal phase-field profiles

In a general setting in 1D, we seek for v that minimizes

$$\int_0^\infty G_\mathrm{c}(x) S(v, \nabla v)\,\mathrm{d}x := \int_0^\infty \frac{G_\mathrm{c}(x)}{4c_n}\left(\frac{(1-v)^n}{\ell} + \ell|v'|^2\right)\mathrm{d}x \tag{45}$$

where c_n is the normalizing parameter given by $c_n := \int_0^1 (1-\omega)^{n/2}\mathrm{d}\omega$. In the followings, we derive the optimal profile of v for $\mathtt{AT}_1$ ($n = 1$) and $\mathtt{AT}_2$ ($n = 2$) when $G_\mathrm{c}(x)$ is a piecewise constant as defined in (13).

6.1.1. Optimal profile for $\mathtt{AT}_1$

We follow the procedures outlined in [32] closely in this construction. As discussed in 2.2.3, the diffused length b needs to be within the transition length 2ℓ. For $b < 2\ell$ and $x \in (0, b)$, a general solution to the Euler-Lagrange equation is given as:

$$v(x) = \begin{cases} -\dfrac{1}{4\ell^2}x^2 + \beta_1 x + \beta_3 & \text{for } \ 0 \leq x \leq b, \\ -\dfrac{1}{4\ell^2}x^2 + \beta_2 x + \beta_4 & \text{for } \ b \leq x. \end{cases} \tag{46}$$

To solve for β_1, β_2, β_3, and β_4, we use: (1) $v(x) = 0$ at $x = 0$, (2) the continuity of $v(x)$ at $x = b$, (3) the first Weierstrass-Erdmann corner condition[6], (4) the inequality conditions $v(x) \leq 1$, and (5) $v'(x) \geq 0$.

From the boundary condition $v(0) = 0$, we have

$$\beta_3 = 0. \tag{47}$$

For the continuity at b, $v(b-0) = v(b+0)$, we get

$$\beta_4 = b(\beta_1 - \beta_2). \tag{48}$$

Substituting (48) into (46) gives

$$v(x) = -\frac{1}{4\ell^2}(x - 2\ell^2\beta_2)^2 + \ell^2\beta_2^2 + b(\beta_1 - \beta_2). \tag{49}$$

This is a negative parabola attaining the maximum abscissa of $\ell^2\beta_2^2 + b(\beta_1 - \beta_2)$ at $x = 2\ell^2\beta_2$. Since $x > 0$, we have

$$\beta_2 \geq 0. \tag{50}$$

As the inequality condition requires that $v(x) \leq 1$, we have $\ell^2\beta_2^2 + b(\beta_1 - \beta_2) \leq 1$. Furthermore, to meet the inequality $v'(x) \geq 0$, we need the parabola to reach the maximum value of 1 at $x = 2\ell^2\beta_2$. Thus we have the limit case of:

$$\ell^2\beta_2^2 + b(\beta_1 - \beta_2) = 1. \tag{51}$$

Finally, applying the first Weierstrass-Erdmann corner condition, $\tilde{G}_\mathrm{c}^\mathrm{int} v'|_{x=b-0} = G_\mathrm{c}^\mathrm{bulk} v'|_{x=b+0}$, we get β_1 as in (24). Then from (50), (51) and (24), we obtain β_2 as in (25).

[6] The second condition is required when b is unknown.

6.1.2. Optimal profile for $\mathtt{AT}_2$

Similarly to the $\mathtt{AT}_1$ case, a general solution for the phase-field profile is given by:

$$v(x) = \begin{cases} 1 - \alpha_1 e^{-x/\ell} - \alpha_3 e^{x/\ell} & \text{for } \ 0 \le x \le b, \\ 1 - \alpha_2 e^{-x/\ell} - \alpha_4 e^{x/\ell} & \text{for } \ b \le x. \end{cases} \tag{52}$$

We can solve for α_1, α_2, α_3, and α_4, using the boundary conditions of (1) $v = 0$ at $x = 0$ and (2) $v = 1$ with $x \to \infty$, (3) the first Weierstrass-Erdmann condition, and (4) the continuity of v.

From $v(0) = 0$, we have

$$\alpha_3 = 1 - \alpha_1. \tag{53}$$

Applying $v(\infty) \to 1$ yields

$$\alpha_4 = 0. \tag{54}$$

The first Weierstrass-Erdmann condition provides

$$\tilde{G}_{\mathrm{c}}^{\mathrm{int}} \left\{ \alpha_1 e^{-x/\ell} - (1 - \alpha_1) e^{x/\ell} \right\} = G_{\mathrm{c}}^{\mathrm{bulk}} \alpha_2 e^{-x/\ell}. \tag{55}$$

Finally the continuity of v at $x = b$ imposes

$$\alpha_1 e^{-x/\ell} + (1 - \alpha_1) e^{x/\ell} = \alpha_2 e^{-x/\ell}. \tag{56}$$

From (55) and (56), we obtain (18).

6.2. Limits of the effective interface fracture toughness

The effective interface fracture toughness proposed in this study are bounded in $(0, G_{\mathrm{c}}^{\mathrm{int}})$ with the limits of b/ℓ.

For $\mathtt{AT}_1$, as $b \to 0$ $(b/\ell \to 0)$, we have that

$$\beta_1 \to \frac{G_{\mathrm{c}}^{\mathrm{bulk}}}{\tilde{G}_{\mathrm{c}}^{\mathrm{int}}} \beta_2 \quad \text{and} \quad \beta_2 \to \frac{1}{\ell}. \tag{57}$$

Applying (57) to (28) and (29) gives

$$\gamma_1 \to 0 \quad \text{and} \quad \gamma_2 \to \frac{4}{3}. \tag{58}$$

Therefore, we obtain $G_{\mathrm{c}}^{\mathrm{int}} \to G_{\mathrm{c}}^{\mathrm{bulk}}$ and $\tilde{G}_{\mathrm{c}}^{\mathrm{int}} \to 0$.

For the upper bound ($b/\ell \to \infty$ or $\ell \to 0$), since $b < 2\ell$, it is given as $b/\ell \to 2$. As we send $b \to 2\ell$, we get

$$\beta_1 \to \frac{1}{\ell} \quad \text{and} \quad \beta_2 \to \frac{1}{\ell}. \tag{59}$$

Similarly, applying (59) to (28) and (29), we have

$$\gamma_1 \to \frac{4}{3} \quad \text{and} \quad \gamma_2 \to 0. \tag{60}$$

Therefore, from (27), we obtain $G_{\mathrm{c}}^{\mathrm{int}} \to \tilde{G}_{\mathrm{c}}^{\mathrm{int}}$.

For $\mathtt{AT}_2$, as we send $b \to 0$, we have

$$\alpha_1^2 \left(1 - e^{-2b/\ell}\right) \to 0 \quad \text{and} \quad \left(1 - \alpha_1^2\right) \left(1 - e^{2b/\ell}\right) \to 0, \tag{61}$$

and

$$\alpha_2^2 e^{-2b/\ell} \to 1. \tag{62}$$

Substituting (61) and (62) into (20), we have $G_\mathrm{c}^\mathrm{int} \to G_\mathrm{c}^\mathrm{bulk}$ and $\tilde{G}_\mathrm{c}^\mathrm{int} \to 0$.

In the upper bound ($b/\ell \to \infty$), we have

$$\alpha_1^2 \left(1 - e^{-2b/\ell}\right) \to 1 \quad \text{and} \quad \left(1 - \alpha_1^2\right) \left(1 - e^{2b/\ell}\right) \to 0, \tag{63}$$

and

$$\alpha_2^2 e^{-2b/\ell} \to 0. \tag{64}$$

Putting (63) and (64) into (20) yields $G_\mathrm{c}^\mathrm{int} \to \tilde{G}_\mathrm{c}^\mathrm{int}$.

6.3. Implementation of the variational phase-field model

The phase-field profiles discussed are the optimal profiles that minimize the surface energy without the presence of the strain energy. In a variational phase-field model for fracture, $\mathbf{u}$ and v are obtained through minimization of the Francfort-Marigo energy and no profile of v is imposed a priori. Following [12], the energy functional is regularized as:

$$\mathcal{F}_\ell := \int_\Omega v^2 W(\mathbf{u}) \,\mathrm{d}\Omega + \int_\Omega \frac{G_\mathrm{c}}{4c_n} \left(\frac{(1-v)^n}{\ell} + \ell |\nabla v|^2 \right) \mathrm{d}\Omega. \tag{65}$$

The strain energy is computed using a linearized strain, $\boldsymbol{\varepsilon}(\mathbf{u}) := (\nabla \mathbf{u} + \nabla \mathbf{u}^\mathrm{T})/2$, as:

$$W(\mathbf{u}) = \frac{1}{2} \mathbf{C} : \boldsymbol{\varepsilon}(\mathbf{u}) : \boldsymbol{\varepsilon}(\mathbf{u}), \tag{66}$$

where $\mathbf{C}$ is the fourth order linear elastic tangent operator.

Although the importance of splitting the strain energy into tension and compression parts have been discussed by [5, 31, 62, 75, 77], the isotropic strain energy as in the original model [12] is sufficient to recover the closed form solutions for tensile dominant fracture in the verification examples in Section 3[7].

In a discrete time series, we obtain $\mathbf{u}_i$ and v_i at a given time t_i by minimizing:

$$(\mathbf{u}_i, v_i) = \operatorname{argmin} \left\{ \mathcal{F}_\ell(\mathbf{u}, v) : \mathbf{u} \in \mathcal{U}(t_i), v \in \mathcal{V}(t_i, v_{i-1}) \right\}, \tag{67}$$

where $\mathcal{U}$ is the kinematically admissible displacement set:

$$\mathcal{U}(t_i) = \left\{ \mathbf{u} \in H^1(\Omega) : \mathbf{u} = 0 \quad \text{on} \quad \partial\Omega_D \right\}. \tag{68}$$

The kinematically admissible set of v requires an irreversible condition. We adopt the irreversible condition introduced by [12, 13] where we set $v(x) = 0$ in:

$$\mathrm{CR}(t_{i-1}) := \left\{ x \in \Omega : v_{i-1} \le \eta \right\}, \tag{69}$$

[7] In Section 4, as the pre-scribed interface undergoes compression, we applied the strain energy split based on a spectral decomposition [62].

where η is a threshold. $\eta = 1$ corresponds to a strict irreversibility *i.e.* $0 \leq v(x) \leq v_{i-1}$ whereas $\eta \simeq 0$ corresponds to a "soft" irreversibility which allows the material to heal unless fully broken. Thus we have:

$$\mathcal{V}(t_i, v_{i-1}) = \left\{ v \in H^1(\Omega) : v = 0 \quad \text{on} \quad \mathrm{CR}(t_{i-1}) \right\}. \tag{70}$$

Taking advantage of the bi-convexity of (65), we solve the system by alternatively minimizing (65) with respect to $\mathbf{u}$ and v. As the solution of v requires a variational inequality, we use a non-linear solver provided by PETSc [7, 8]. Alternative ways to impose the irreversibility include an augmented Lagrangian approach [81], use of history variable [2, 62], or a penalty based method [32].

The present model is implemented in an open source code, OpenGeoSys [9]. Further information on the code and simulation examples are freely accessible at https://www.opengeosys.org/.

6.4. Variational phase-field model for hydraulic fracture

We extend the total energy function by adding the work done by the fluid pressure, $\int_\Gamma p_f \llbracket \mathbf{u} \cdot \mathbf{n} \rrbracket \, \mathrm{d}\Gamma$, where p_f is the "net" pressure defined as the excess pressure above the minimum stress and $\mathbf{n}$ is the normal vector to Γ. The jump quantity over Γ can be approximated as [11, 21]:

$$\int_\Gamma p_f \llbracket \mathbf{u} \cdot \mathbf{n} \rrbracket \, \mathrm{d}\Gamma \approx \int_\Omega p_f \, \mathbf{u} \cdot \nabla v \, \mathrm{d}\Omega.$$

As the toughness dominated hydraulic fracturing regime considers no pressure loss in the crack, our total energy yields as:

$$\mathcal{E}_\ell := \int_\Omega v^2 W(\mathbf{u}) \, \mathrm{d}\Omega + \int_\Omega \frac{G_\mathrm{c}}{4c_n} \left(\frac{(1-v)^n}{\ell} + \ell |\nabla v|^2 \right) \mathrm{d}\Omega + p_f \int_\Omega \mathbf{u} \cdot \nabla v \, \mathrm{d}\Omega. \tag{71}$$

Unlike boundary load driven fracture where the boundary displacement is controlled with time (*e.g.* the surfing example), hydraulic fracture is driven by fluid volume changes in the system. Without fluid leak-off from the crack, the injected volume Q_i at $t = t_i$ is equal to the crack volume $V := \int_\Omega \mathbf{u} \cdot \nabla v \, \mathrm{d}\Omega$. Thus we minimize (71) with this mass balance constrain as:

$$(\mathbf{u}_i, v_i; p_f) = \operatorname{argmin} \left\{ \mathcal{E}_\ell(\mathbf{u}, v; p) : \mathbf{u} \in \mathcal{U}(t_i), v \in \mathcal{V}(t_i, v_{i-1}), Q_i = \int_\Omega \mathbf{u} \cdot \nabla v \, \mathrm{d}\Omega \right\}. \tag{72}$$

References

[1] Alessi, R., Marigo, J.-J., Maurini, C., and Vidoli, S. (2018). Coupling damage and plasticity for a phase-field regularisation of brittle, cohesive and ductile fracture: One–dimensional examples. *International Journal of Mechanical Sciences*, 149:559–576.

[2] Ambati, M., Gerasimov, T., and De Lorenzis, L. (2014). A review on phase-field models of brittle fracture and a new fast hybrid formulation. *Computational Mechanics*, 55(2):383–405.

[3] Ambati, M., Gerasimov, T., and De Lorenzis, L. (2015). Phase-field modeling of ductile fracture. *Computational Mechanics*, 55(5):1017–1040.

[4] Ambrosio, L. and Tortorelli, V. M. (1992). On the approximation of free discontinuity problems. *Boll. Un. Mat. Ital. B (7)*, 6(1):105–123.

[5] Amor, H., Marigo, J.-J., and Maurini, C. (2009). Regularized formulation of the variational brittle fracture with unilateral contact: Numerical experiments. *Journal of the Mechanics and Physics of Solids*, 57(8):1209–1229.

[6] Anderson, T. L. (2017). *Fracture mechanics: fundamentals and applications*. CRC press.

[7] Balay, S., Abhyankar, S., Adams, M. F., Brown, J., Brune, P., Buschelman, K., Dalcin, L., Dener, A., Eijkhout, V., Gropp, W. D., Karpeyev, D., Kaushik, D., Knepley, M. G., May, D. A., McInnes, L. C., Mills, R. T., Munson, T., Rupp, K., Sanan, P., Smith, B. F., Zampini, S., Zhang, H., and Zhang, H. (2020). PETSc users manual. Technical Report ANL-95/11 - Revision 3.13, Argonne National Laboratory.

[8] Balay, S., Abhyankar, S., Adams, M. F., Brown, J., Brune, P., Buschelman, K., Dalcin, L., Dener, A., Eijkhout, V., Gropp, W. D., Karpeyev, D., Kaushik, D., Knepley, M. G., May, D. A., McInnes, L. C., Mills, R. T., Munson, T., Rupp, K., Sanan, P., Smith, B. F., Zampini, S., Zhang, H., and Zhang, H. (2019). PETSc Web page.

[9] Bilke, L., Flemisch, B., Kalbacher, T., Kolditz, O., Helmig, R., and Nagel, T. (2019). Development of Open-Source Porous Media Simulators: Principles and Experiences. *Transport in Porous Media*, 130(1):337–361.

[10] Borden, M., Verhoosel, C., Scott, M., Hughes, T., and Landis, C. (2012). A phase-field description of dynamic brittle fracture. *Computer Methods in Applied Mechanics and Engineering*, 217-220:77–95.

[11] Bourdin, B., Chukwudozie, C., and Yoshioka, K. (2012). A variational approach to the numerical simulation of hydraulic fracturing. In *SPE Annual Technical Conference and Exhibition*. Society of Petroleum Engineers.

[12] Bourdin, B., Francfort, G., and Marigo, J.-J. (2000). Numerical experiments in revisited brittle fracture. *J. Mech. and Phys. of Solids*, 48(4):797–826.

[13] Bourdin, B., Francfort, G., and Marigo, J.-J. (2008). The variational approach to fracture. *Journal of Elasticity*, 91(1-3):5–148.

[14] Bourdin, B., Larsen, C., and Richardson, C. (2011). A time-discrete model for dynamic fracture based on crack regularization. *International Journal of Fracture*, 168(2):133–143.

[15] Bourdin, B., Marigo, J. J., Maurini, C., and Sicsic, P. (2014). Morphogenesis and propagation of complex cracks induced by thermal shocks. *Physical Review Letters*, 112(1):1–5.

[16] Braides, A. (1998). *Approximation of Free-Discontinuity Problems*. Number 1694 in Lecture Notes in Mathematics. Springer.

[17] Cajuhi, T., Sanavia, L., and De Lorenzis, L. (2018). Phase-field modeling of fracture in variably saturated porous media. *Computational Mechanics*, 61(3):299–318.

[18] Carrara, P., Ambati, M., Alessi, R., and De Lorenzis, L. (2020). A framework to model the fatigue behavior of brittle materials based on a variational phase-field approach. *Computer Methods in Applied Mechanics and Engineering*, 361:112731.

[19] Chambolle, A., Francfort, G. A., and Marigo, J.-J. (2009). When and how do cracks propagate? *Journal of the Mechanics and Physics of Solids*, 57(9):1614–1622.

[20] Choo, J. and Sun, W. (2018). Cracking and damage from crystallization in pores: Coupled chemo–hydro–mechanics and phase–field modeling. *Computer Methods in Applied Mechanics and Engineering*, 335:347–379.

[21] Chukwudozie, C., Bourdin, B., and Yoshioka, K. (2019). A variational phase-field model for hydraulic fracturing in porous media. *Computer Methods in Applied Mechanics and Engineering*, 347:957–982.

[22] Chuprakov, D., Melchaeva, O., and Prioul, R. (2014). Injection-sensitive mechanics of hydraulic fracture interaction with discontinuities. *Rock Mechanics and Rock Engineering*, 47(5):1625–1640.

[23] Cui, C., Ma, R., and Martínez-Pañeda, E. (2021). A phase field formulation for dissolution-driven stress corrosion cracking. *Journal of the Mechanics and Physics of Solids*, 147:104254.

[24] Dahi-Taleghani, A. and Olson, J. E. (2011). Numerical Modeling of Multistranded-Hydraulic-Fracture Propagation: Accounting for the Interaction Between Induced and Natural Fractures. *SPE Journal*, 16(03):575–581.

[25] Dean, R. H. and Schmidt, J. H. (2009). Hydraulic-fracture predictions with a fully coupled geomechanical reservoir simulator. *SPE Journal*, 14(04):707–714.

[26] Donnini, J., Lancioni, G., and Corinaldesi, V. (2018). Failure modes in frcm systems with dry and pre-impregnated carbon yarns: Experiments and modeling. *Composites Part B: Engineering*, 140:57–67.

[27] Dubois, F., Chazal, C., and Petit, C. (1998). A finite element analysis of creep-crack growth in viscoelastic media. *Mechanics Time-Dependent Materials*, 2(3):269–286.

[28] Ehlers, W. and Luo, C. (2017). A phase-field approach embedded in the Theory of Porous Media for the description of dynamic hydraulic fracturing. *Computer Methods in Applied Mechanics and Engineering*, 315:348–368.

[29] Francfort, G. A. and Marigo, J.-J. (1998). Revisiting brittle fracture as an energy minimization problem. *Journal of the Mechanics and Physics of Solids*, 46(8):1319–1342.

[30] Freddi, F. (2019). Fracture energy in phase field models. *Mechanics Research Communications*, 96:29 – 36.

[31] Freddi, F. and Royer-Carfagni, G. (2010). Regularized variational theories of fracture: A unified approach. *Journal of the Mechanics and Physics of Solids*, 58(8):1154–1174.

[32] Gerasimov, T. and Lorenzis, L. D. (2019). On penalization in variational phase-field models of brittle fracture. *Computer Methods in Applied Mechanics and Engineering*, 354:990–1026.

[33] Gu, H., Weng, X., Lund, J., MacK, M., Ganguly, U., and Suarez-Rivera, R. (2012). Hydraulic fracture crossing natural fracture at nonorthogonal angles: A criterion and its validation. *SPE Production and Operations*, 27(1):20–26.

[34] Gupta, P. and Duarte, C. A. (2014). Simulation of non-planar three-dimensional hydraulic fracture propagation. *International Journal for Numerical and Analytical Methods in Geomechanics*, 38(13):1397–1430.

[35] Hansen-Dörr, A. C., Damma, F., de Borst, R., and Kästner, M. (2020a). Erratum to phase-field modeling of crack branching and deflection in heterogeneous media [eng. fract. mech. 232 (2020) 107004]. *Engineering Fracture Mechanics*, page 107449.

[36] Hansen-Dörr, A. C., Damma, F., de Borst, R., and Kästner, M. (2020b). Phase-field modeling of crack branching and deflection in heterogeneous media. *Engineering Fracture Mechanics*, 232:107004. Erratum: [35].

[37] Hansen-Dörr, A. C., de Borst, R., Hennig, P., and Kästner, M. (2019). Phase-field modelling of interface failure in brittle materials. *Computer Methods in Applied Mechanics and Engineering*, 346:25–42.

[38] He, M.-Y. and Hutchinson, J. W. (1989). Crack deflection at an interface between dissimilar elastic materials. *International Journal of Solids and Structures*, 25(9):1053–1067.

[39] Heider, Y. and Markert, B. (2017). A phase-field modeling approach of hydraulic fracture in saturated porous media. *Mechanics Research Communications*, 80:38–46.

[40] Heider, Y. and Sun, W. (2020). A phase field framework for capillary-induced fracture in unsaturated porous media: Drying-induced vs. hydraulic cracking. *Computer Methods in Applied Mechanics and Engineering*, 359:112647.

[41] Hossain, M. Z., Hsueh, C. J., Bourdin, B., and Bhattacharya, K. (2014). Effective toughness of heterogeneous media. *Journal of the Mechanics and Physics of Solids*, 71(1):15–32.

[42] Hutchinson, J. W. and Suo, Z. (1991). Mixed mode cracking in layered materials. In *Advances in applied mechanics*, volume 29, pages 63–191. Elsevier.

[43] Jeffrey, R., Weber, C., et al. (1994). Hydraulic fracturing experiments in the great northern coal seam. In *SPE Asia Pacific Oil and Gas Conference*, pages 361–371. Society of Petroleum Engineers.

[44] Jeffrey, R., Zhang, X., and Chen, Z. (2017). Hydraulic fracture growth in naturally fractured rock. In *Porous rock fracture mechanics*, pages 93–116. Elsevier.

[45] Ji, L., Settari, A., and Sullivan, R. B. (2009). A novel hydraulic fracturing model fully coupled with geomechanics and reservoir simulation. *SPE Journal*, 14(3):423–430.

[46] Kuhn, C., Noll, T., and Müller, R. (2016). On phase field modeling of ductile fracture. *GAMM Mitteilungen*, 39(1):35–54.

[47] Lee, S. and Wheeler, M. F. (2020). Modeling interactions of natural and two-phase fluid-filled fracture propagation in porous media. *Computational Geosciences*, pages 1–25.

[48] Lee, S., Wheeler, M. F., and Wick, T. (2016). Pressure and fluid-driven fracture propagation in porous media using an adaptive finite element phase field model. *Computer Methods in Applied Mechanics and Engineering*, 312:509–541.

[49] Lepillier, B., Yoshioka, K., Parisio, F., Bakker, R., and Bruhn, D. (2020). Variational Phase-Field Modeling of Hydraulic Fracture Interaction With Natural Fractures and Application to Enhanced Geothermal Systems. *Journal of Geophysical Research: Solid Earth*, 125(7).

[50] Li, B. and Maurini, C. (2019). Crack kinking in a variational phase-field model of brittle fracture with strongly anisotropic surface energy. *Journal of the Mechanics and Physics of Solids*, 125:502–522.

[51] Li, G., Yin, B., Zhang, L., and Liew, K. (2020a). Modeling microfracture evolution in heterogeneous composites: A coupled cohesive phase-field model. *Journal of the Mechanics and Physics of Solids*, 142:103968.

[52] Li, P., Yvonnet, J., and Combescure, C. (2020b). An extension of the phase field method to model interactions between interfacial damage and brittle fracture in elastoplastic composites. *International Journal of Mechanical Sciences*, 179:105633.

[53] Li, T., Marigo, J.-J., Guilbaud, D., and Potapov, S. (2016a). Gradient damage modeling of brittle fracture in an explicit dynamics context. *International Journal for Numerical Methods in Engineering*, 108(11):1381–1405.

[54] Li, T., Marigo, J.-J., Guilbaud, D., and Potapov, S. (2016b). Numerical investigation of dynamic brittle fracture via gradient damage models. *Advanced Modeling and Simulation in Engineering Sciences*, 3(1):1–24.

[55] Liu, Z., Chen, M., and Zhang, G. (2014). Analysis of the influence of a natural fracture network on hydraulic fracture propagation in carbonate formations. *Rock Mechanics and Rock Engineering*, 47(2):575–587.

[56] Longuski, J. M., Guzmán, J. J., and Prussing, J. E. (2014). *Optimal control with aerospace applications*. Springer.

[57] Martínez-Pañeda, E., Golahmar, A., and Niordson, C. F. (2018). A phase field formulation for hydrogen assisted cracking. *Computer Methods in Applied Mechanics and Engineering*, 342:742–761.

[58] Maurini, C., Bourdin, B., Gauthier, G., and Lazarus, V. (2013). Crack patterns obtained by unidirectional drying of a colloidal suspension in a capillary tube: Experiments and numerical simulations using a two-dimensional variational approach. *International Journal of Fracture*, 184(1-2):75–91.

[59] McClure, M. W. and Horne, R. N. (2014). An investigation of stimulation mechanisms in enhanced geothermal systems. *International Journal of Rock Mechanics and Mining Sciences*, 72:242–260.

[60] Meng, C., De Pater, C., et al. (2010). Hydraulic fracture propagation in pre-fractured natural rocks. In *44th US Rock Mechanics Symposium and 5th US-Canada Rock Mechanics Symposium*. American Rock Mechanics Association.

[61] Mesgarnejad, A., Bourdin, B., and Khonsari, M. (2015). Validation simulations for the variational approach to fracture. *Computer Methods in Applied Mechanics and Engineering*, 290:420–437.

[62] Miehe, C., Hofacker, M., and Welschinger, F. (2010). A phase field model for rate-independent crack propagation: Robust algorithmic implementation based on operator splits. *Computer Methods in Applied Mechanics and Engineering*, 199(45):2765–2778.

[63] Mikelić, A., Wheeler, M., and Wick, T. (2019). Phase-field modeling through iterative splitting of hydraulic fractures in a poroelastic medium. *GEM-International Journal on Geomathematics*, 10(1):2.

[64] Nguyen, T. T., Yvonnet, J., Bornert, M., and Chateau, C. (2016a). Initiation and propagation of complex 3D networks of cracks in heterogeneous quasi-brittle materials: Direct comparison between in situ testing-micro CT experiments and phase field simulations. *Journal of the Mechanics and Physics of Solids*, 95:320–350.

[65] Nguyen, T. T., Yvonnet, J., Zhu, Q.-Z., Bornert, M., and Chateau, C. (2016b). A phase-field method for computational modeling of interfacial damage interacting with crack propagation in realistic microstructures obtained by microtomography. *Computer Methods in Applied Mechanics and Engineering*, 312:567–595.

[66] Nguyen, V. P. and Wu, J.-Y. (2018). Modeling dynamic fracture of solids with a phase-field regularized cohesive zone model. *Computer Methods in Applied Mechanics and Engineering*, 340:1000–1022.

[67] Ni, L., Zhang, X., Zou, L., and Huang, J. (2020a). Phase-field modeling of hydraulic fracture network propagation in poroelastic rocks. *Computational Geosciences*.

[68] Ni, T., Pesavento, F., Zaccariotto, M., Galvanetto, U., Zhu, Q. Z., and Schrefler, B. A. (2020b). Hybrid FEM and peridynamic simulation of hydraulic fracture propagation in saturated porous media. *Computer Methods in Applied Mechanics and Engineering*, 366.

[69] Paggi, M. and Reinoso, J. (2017). Revisiting the problem of a crack impinging on an interface: a modeling framework for the interaction between the phase field approach for brittle fracture and the interface cohesive zone model. *Computer Methods in Applied Mechanics and Engineering*, 321:145–172.

[70] Pham, K., Amor, H., Marigo, J.-J., and Maurini, C. (2011). Gradient damage models and their use to approximate brittle fracture. *Int. J. Damage Mech.*, 20(4, SI):618–652.

[71] Santillán, D., Juanes, R., and Cueto-Felgueroso, L. (2017). Phase field model of fluid-driven fracture in elastic media: Immersed-fracture formulation and validation with analytical solutions. *Journal of Geophysical Research: Solid Earth*, 122(4):2565–2589.

[72] Schuler, L., Ilgen, A. G., and Newell, P. (2020). Chemo-mechanical phase-field modeling of dissolution-assisted fracture. *Computer Methods in Applied Mechanics and Engineering*, 362:112838.

[73] Seiler, M., Hantschke, P., Brosius, A., and Kästner, M. (2018). A numerically efficient phase-field model for fatigue fracture–1D analysis. *PAMM*, 18(1):e201800207.

[74] Sneddon, I. and Lowengrub, M. (1969). *Crack problems in the classical theory of elasticity.* The SIAM series in Applied Mathematics. John Wiley & Sons.

[75] Steinke, C. and Kaliske, M. (2019). A phase-field crack model based on directional stress decomposition. *Computational Mechanics*, 63(5):1019–1046.

[76] Strobl, M. and Seelig, T. (2015). A novel treatment of crack boundary conditions in phase field models of fracture. *PAMM*, 15(1):155–156.

[77] Strobl, M. and Seelig, T. (2020). Phase field modeling of Hertzian indentation fracture. *Journal of the Mechanics and Physics of Solids*, 143:104026.

[78] Tanné, E. (2017). *Variational phase-field models from brittle to ductile fracture: nucleation and propagation.* PhD thesis, Université Paris-Saclay (ComUE).

[79] Tanné, E., Li, T., Bourdin, B., Marigo, J.-J., and Maurini, C. (2018). Crack nucleation in variational phase-field models of brittle fracture. *J. Mech. Phys. Solids*, 110:80–99.

[80] Vahab, M., Hirmand, M., Jafari, A., and Khalili, N. (2021). Numerical analysis of multiple hydro-fracture growth in layered media based on a non-differentiable energy minimization approach. *Engineering Fracture Mechanics*, 241:107361.

[81] Wheeler, M., Wick, T., and Wollner, W. (2014). An augmented-Lagrangian method for the phase-field approach for pressurized fractures. *Computer Methods in Applied Mechanics and Engineering*, 271:69–85.

[82] Wu, J.-Y. (2017). A unified phase-field theory for the mechanics of damage and quasi-brittle failure. *Journal of the Mechanics and Physics of Solids*, 103:72–99.

[83] Xu, L. R., Huang, Y. Y., and Rosakis, A. J. (2003). Dynamic crack deflection and penetration at interfaces in homogeneous materials: experimental studies and model predictions. *Journal of the Mechanics and Physics of Solids*, 51(3):461–486.

[84] Yew, C. H. and Weng, X. (2014). *Mechanics of hydraulic fracturing.* Gulf Professional Publishing.

[85] Yin, B. and Kaliske, M. (2020). A ductile phase-field model based on degrading the fracture toughness: Theory and implementation at small strain. *Computer Methods in Applied Mechanics and Engineering*, 366:113068.

[86] Yoshioka, K. and Bourdin, B. (2016). A variational hydraulic fracturing model coupled to a reservoir simulator. *International Journal of Rock Mechanics and Mining Sciences*, 88:137–150.

[87] Yoshioka, K., Naumov, D., and Kolditz, O. (2020). On crack opening computation in variational phase-field models for fracture. *Computer Methods in Applied Mechanics and Engineering*, 369:113210.

[88] Zhao, Y., Zhang, Y. F., and He, P. F. (2019). A composite criterion to predict subsequent intersection behavior between a hydraulic fracture and a natural fracture. *Engineering Fracture Mechanics*, 209(March):61–78.

[89] Zimmermann, N. and Wang, P. H. (2020). A review of failure modes and fracture analysis of aircraft composite materials. *Engineering Failure Analysis*, 115:104692.